Standardized daily high-resolution large-eddy simulations of the Arctic boundary layer and clouds during the complete *MOSAiC* drift

N. Schnierstein[1], J. Chylik[1], M. D. Shupe[2,3], R. A. J. Neggers[1]

[1]Institute for Geophysics and Meteorology, University of Cologne, Cologne, Germany
[2]Physical Sciences Laboratory, National Oceanic and Atmospheric Administration, Boulder, CO, USA
[3]Cooperative Institute for Research in Environmental Sciences, University of Colorado, Boulder, CO, USA

Key Points:

- Campaign data is deeply integrated into the experimental design of daily turbulence- and cloud-resolving simulations.
- Independent drift-long statistics on key aspects of the surface energy budget, thermodynamic structure, and clouds are reproduced.
- Sensitivities of the results to the experimental design and model physics are explored.

Corresponding author: Niklas Schnierstein, `nschnier@uni-koeln.de`

Abstract

This study utilizes the wealth of observational data collected during the recent *MOSAiC* drift experiment to constrain and evaluate 190 daily Large-Eddy Simulations (LES) of Arctic boundary layers and clouds at turbulence-resolving resolutions. A standardized approach is adopted to tightly integrate field measurements into the experimental configuration. Covering the full drift represents a step forward from single-case LES studies, and allows for a robust assessment of model performance against independent data under a broad range of atmospheric conditions. A homogeneously forced Eulerian domain is simulated, initialized with radiosonde and value-added cloud profiles. Prescribed boundary conditions include various measured surface characteristics. Time-constant composite forcing is applied, primarily consisting of subsidence rates sampled from reanalysis data. The simulations run for multiple hours, allowing turbulence and mixed-phase clouds to spin up while still facilitating direct comparison to *MOSAiC* data. Key aspects such as the vertical thermodynamic structure, cloud properties, and surface energy fluxes are satisfactorily reproduced and maintained. Specifically, the model captures the bimodal distribution of atmospheric states that is typical of Arctic climate. Selected days are investigated more closely to assess the model's skill in maintaining the observed boundary layer structure. The sensitivity to various aspects of the experimental configuration and model physics is tested. The model input and output are available to the scientific community, supplementing the *MOSAiC* data archive. The close agreement with observed meteorology justifies the use of LES data for gaining further insight into Arctic processes and their role in Arctic climate change.

Plain Language Summary

The Arctic is one of the regions most affected by global climate change, warming up to four times as fast as the rest of the globe. It is also a particularly inaccessible region to conduct measurements. Fortunately, between 2019 and 2020 the *MOSAiC* campaign collected an unprecedented amount of data in the Arctic. In this study, numerous of these measurements are incorporated into high-resolution computer simulations of the lowest part of the Arctic atmosphere. This simulation data complements and contextualizes the observations and enables insight into complex physical processes, e.g., cloud formation, ice production, or turbulent mixing. The Arctic is an extreme place, and models often struggle to represent the atmosphere accurately. Therefore, the main achievement of this study is to successfully simulate 190 atmospheric situations as measured during the campaign. The generated data set performs well when compared to independent observations. Single cases deliver information about individual atmospheric conditions, and the collection gives insight into how key climate variables behaved throughout the *MOSAiC* year.

1 Introduction

The ongoing rapid warming of the Arctic region is a significant contributor to global climate change. Due to amplification processes, the Arctic warms up to four times as fast as the rest of the globe (Serreze & Barry, 2011; Rantanen et al., 2022). Past research suggests various feedback processes cause this Arctic Amplification (AA) (Wendisch et al., 2023), including the albedo (Screen & Simmonds, 2010; Thackeray & Hall, 2019; Dai et al., 2019; Jenkins & Dai, 2021), Planck (Pithan & Mauritsen, 2014), water-vapor, lapse rate (Stuecker et al., 2018; Linke et al., 2023), and cloud feedback (Philipp et al., 2020; Middlemas et al., 2020). To better understand these feedback mechanisms, it is crucial to quantify the effects of turbulent boundary layer processes in the Arctic atmosphere amid a changing climate (Taylor et al., 2018). Furthermore, it is essential to inform large-scale model parameterizations with high-resolution modeling efforts. Here, a collection of 190 of these numerical experiments is created by integrating a variety of Arctic measurements.

The investigation of the high Arctic is highly challenging for various reasons. The dynamic sea-ice masses make it impossible to install permanent measuring stations. Therefore, reliable meteorological data from ship- and airborne measurement campaigns and satellite imagery is sparsely available. All of which suffer from spatial and temporal gaps in the coverage. The *Multidisciplinary drifting Observatory for the Study of Arctic Climate* (*MOSAiC*, Shupe et al. (2020)) was a major international field campaign that took place in the Arctic from September 2019 to October 2020, intending to fill essential data gaps in in-situ observations in the central Arctic, covering an entire annual cycle. The campaign involved the deployment of the German research vessel *Polarstern*, which was frozen into the Arctic sea ice and drifted with it for over a year. During this time, the campaign and connected projects gathered an unprecedented amount of highly diverse data sets and made them available to the research communities in atmospheric, cryospheric, and oceanic sciences (Shupe et al., 2022; Nicolaus et al., 2022; Rabe et al., 2022).

The first objective of this work is to integrate available observational data sets from the *MOSAiC* campaign into a high-resolution numerical experiment. This supplements the data record with time-resolved three-dimensional modeling results and augments singular data sets by contextualizing their role in a turbulent boundary layer. A quantity of high-resolution Large Eddy Simulations (LES) are performed to achieve this.

LES is valuable for resolving critical small-scale boundary layer processes, including cloud dynamics and turbulence. This method also employs well-established parameterization techniques for surface energy exchange and micro-physical processes to facilitate the simulation of larger domains, allowing for the formation of mesoscale structures. LES has been extensively utilized in boundary layer research for several decades - also in the Arctic region. Granted, past model intercomparison studies show weaknesses and strong sensitivities in representing (mixed-phase) cloud properties (Klein et al., 2009; Fridlind et al., 2012; Ovchinnikov et al., 2014; Stevens et al., 2018) and there is strong evidence suggesting a high spatial resolution is needed to accurately represent the turbulent dynamics in a rather energy-sparse Arctic atmosphere (van der Linden et al., 2020; van der Linden & Ansorge, 2022). Nonetheless, there have been several additional successful studies using LES for Arctic boundary layer research (e.g., Solomon et al. (2011); Morrison et al. (2011); Neggers, Chylik, et al. (2019); Egerer et al. (2021); Chylik et al. (2023)): This demonstrates the importance of a careful setup to achieve an accurate representation of the Arctic atmosphere in a virtual domain. The amount of *MOSAiC* datasets enables a setup with a minimum of uncertainties as well as a fair and thorough evaluation of the results.

The overarching goal of this particular work is to create a suit of 190 high-resolution LES representing the conditions of the lower Arctic atmosphere throughout the whole *MOSAiC* year. The choice of days was purely taken based on sufficient data availability. This approach has two main objectives: First, learn about the Arctic climate system, especially smaller-scale processes that are difficult to measure reliably and can hardly be accurately represented in larger-scale models. Second, identify weaknesses in the model under different conditions by evaluating the simulation results against a large amount of diverse *MOSAiC* data sets. Therefore, keeping a standardized setup for each case is crucial to discovering systematic framework or parameterization problems. Initial and boundary conditions, model settings, and evaluation are all done without any manual adjustment on a case-to-case basis. The approach taken in this work sets it apart from individual case studies that prioritize optimizing single simulations at the expense of gaining a broader understanding of the model's potential weaknesses, which a highly customized configuration may mask. It also enables the creation of impact studies for a diverse library of cases by modifying this standardized setup.

The idea of standardized multi-month/multi-year LES has been successfully employed at different super-sites where continuous data is available, e.g., at Cabauw, Netherland (Neggers et al., 2012; Schalkwijk et al., 2015), at JOYCE, Germany (van Laar et al., 2019), within the LASSO project (Gustafson Jr et al., 2020) or even in more northern places as Svalbard (Kiszler et al., 2023). The *Polarstern* and the surrounding measurement stations act as a one-year super-site.

Section 2 gives a detailed description of the method, including an overview of the datasets used, the numerical model framework, and the configuration of the experiments based on the *MOSAiC* data. The results of the simulation and their evaluation against measurements are presented in section 3. A detailed discussion of the results' meaning, implications, and limitations is found in section 4. Finally, section 5 summarizes the main conclusions of this study and provides an outlook on future research it might inspire.

2 Data and Method

2.1 *MOSAiC* datasets

At the foundation of the drift-covering library of high-resolution Large Eddy Simulations of the Arctic atmospheric boundary layer discussed in this study are the observational datasets collected during the *MOSAiC* drift. Table 1 gives a complete overview of these data. It includes the variable, its units and full name, the dimensionality, the associated instrument, and the scientific study presenting the dataset. We refer to these publications for a more detailed technical and scientific description of these datasets and the associated instruments.

Vertical profiles of the thermodynamic state, including temperature and water vapor specific humidity, are provided by the daily 11:00 UTC radiosonde launches during the *MOSAiC* campaign (Maturilli et al., 2022; Dahlke et al., 2023). Vertical cloud liquid and ice water content profiles are obtained from the value-added cloud product based on remote sensing datasets as described by Shupe et al. (2015). Information on cloud condensation nuclei concentrations is based on aerosol measurements (Koontz et al., 2020), while ice nucleating particle concentrations are based on the aerosol measurements by Creamean (2022). The skin temperature of the sea ice is based on the brightness temperature measurements from the *MetCity* location on the sea ice (Cox et al., 2023; Cox et al., 2023). Also based on tower measurements are estimates of the surface aerodynamic roughness length (Gallagher, 2023). Finally, surface albedo values are obtained from satellite products (Spreen et al., 2008; Istomina et al., 2020).

A few datasets required for the configuration of the daily numerical experiments are not mentioned in Table 1 because they are based on *ERA5* reanalysis data (Hersbach et al., 2018a, 2018b, 2023). These include vertical profiles of horizontal wind and time series of the sea-ice fraction. The motivation for using reanalysis products for these variables is to make the simulated domain reflect a larger area and avoid introducing ultralocal effects. A few variables are also derived from *ERA5* because they were not measured during the *MOSAiC* drift. These include large-scale vertical motion (subsidence) and pressure gradients, adopting the procedure implemented by Neggers, Chylik, et al. (2019); van Laar et al. (2019).

The resulting simulations are evaluated against additional *MOSAiC* datasets independent from those used in the experimental design. Simulated short- and longwave radiative fluxes are compared to sensor data of the radiation station described by Cox et al. (2023) and Riihimaki (2021). This installation was part of *MetCity* with sensors placed at 3 m (upwelling) and 1.5 m (downwelling) height. Simulated near-surface turbulent heat fluxes are evaluated against data described by Cox et al. (2023), who discuss two different heat flux datasets. One is directly retrieved from sonic-anemometer turbulence measurements, while the other is a bulk calculation based on Monin-Obukhov theory. The latter is used in this study, although Cox et al. (2023) do mention potential over-simplifications, such as the assumption of constant roughness lengths. Since the surface flux parameterization in the model is also based on Monin-Obukhov theory, the use of bulk measurements yields the fairest comparison of the model to data.

2.2 Model setup

2.2.1 LES code

The *Dutch Large Eddy Simulation* framework (*DALES*, Heus et al. (2010)) was utilized in this research. This code has been effectively employed in numerous boundary layer studies (de Roode et al., 2016; Van der Dussen et al., 2013; van Laar et al., 2019), particularly also to conduct Arctic research (Neggers, Chylik, et al., 2019; de Roode et al., 2019; Chylik et al., 2023; Egerer et al., 2021). The foundation of the model is the Ogura-Phillips anelastic equations for a set of prognostic variables, including liquid water potential temperature Θ_l, the velocity components $\{u, v, w\}$, total water specific humidity q_t, and the mass concentration as well as number concentration of various hydrometeor species. Momentum advection is calculated by a fifth-order central difference scheme and scalar advection by a κ-limiter scheme (Hundsdorfer et al., 1995). A prognostic TKE model calculates the subgrid-scale transport of heat, moisture, and momentum. Finally, the time integration makes use of a 3rd-order Runge-Kutta scheme. To better represent mixed-phase clouds in a wide range of conditions, we enhanced the cloud microphysics scheme, the radiation scheme, and the surface scheme, as described in more detail below.

2.2.2 Microphysics

The mixed-phase, double-moment micro-physics scheme by Seifert and Beheng (2006) has enabled the inclusion of ice-cloud processes in investigations of the Arctic climate system and has been used in various research projects and models (Schemann & Ebell, 2020; Kiszler et al., 2023; Chylik et al., 2023; Linke et al., 2023). It considers the mass and number concentration of five hydro-meteors: Cloud droplets and cloud ice crystals and the precipitating hydro-meteors snow, graupel, and rain. The cloud condensation nuclei concentration is single-species and prognostic, while the ice nucleating particle concentration is also single-species but prescribed, and its activation depends on temperature. The microphysics scheme was initially designed for simulating ice clouds in the mid-latitudes and, therefore, requires evaluation and partial adaptation to suit the extremely cold conditions in the high Arctic. Two key changes to the original implementation (Chylik et al., 2023) were made: Firstly, we calculate the heterogeneous freezing rates using the maximum of the actual atmospheric temperature and $T_\mathrm{het,lim} = -15\,^\circ\mathrm{C}$, as temperatures below this threshold lead to the edges of the valid range of the parameterization being approached and exceeded (Pruppacher & Klett, 1996). Secondly, the maximum number concentration of nucleated ice particles produced by deposition-nucleation is limited to $c_{N,\mathrm{ice}} = 200\,\mathrm{L}^{-1}$ to prevent an unrealistically high concentration of tiny ice particles, which would exceed the estimated concentration of available ice nucleat-

Table 1. Overview of observational data sets utilized to set, constrain, and evaluate the conducted simulations.

Variable	Unit	Description	Dimension	Instrument	Citation
α	%	Surface albedo	(t)	AMSR-E Satellite	Spreen et al. (2008); Istomina et al. (2020)
q_v	$\mathrm{kg\,kg^{-1}}$	Water vapor specific humidity	(z,t)	Radiosonde	Maturilli et al. (2022); Dahlke et al. (2023)
Θ_v	K	Virtual potential temperature	(z,t)	Radiosonde	Maturilli et al. (2022); Dahlke et al. (2023)
q_l	$\mathrm{kg\,kg^{-1}}$	Liquid water specific humidity	(z,t)	Multi-sensor retrieval	Shupe et al. (2015)
q_i	$\mathrm{kg\,kg^{-1}}$	Ice water specific humidity	(z,t)	Multi-sensor retrieval	Shupe et al. (2015)
$\mathrm{LW_d}$	$\mathrm{W\,m^{-2}}$	Longwave downward radiative flux	(t)	Radiation station	Cox et al. (2023); Riihimaki (2021)
$\mathrm{LW_u}$	$\mathrm{W\,m^{-2}}$	Longwave upward radiative flux	(t)	Radiation station	Cox et al. (2023); Riihimaki (2021)
$\mathrm{SW_d}$	$\mathrm{W\,m^{-2}}$	Shortwave downward radiative flux	(t)	Radiation station	Cox et al. (2023); Riihimaki (2021)
$\mathrm{SW_u}$	$\mathrm{W\,m^{-2}}$	Shortwave upward radiative flux	(t)	Radiation station	Cox et al. (2023); Riihimaki (2021)
T_skin	K	Skin temperature	(t)	Radiation station	Cox et al. (2023); Riihimaki (2021)
$U_\mathrm{10\,m}$	$\mathrm{m\,s^{-1}}$	10 m wind speed	(t)	Meteorological tower	Cox et al. (2023); Cox et al. (2023)
$T_\mathrm{10\,m}$	K	10 m temperature	(t)	Meteorological tower	Cox et al. (2023); Cox et al. (2023)
$H_{s,\mathrm{10\,m,bulk}}$	$\mathrm{W\,m^{-2}}$	10 m Bulk sensible heat flux	(t)	Meteorological tower	Cox et al. (2023); Cox et al. (2023)
$H_{s,\mathrm{10\,m,turb}}$	$\mathrm{W\,m^{-2}}$	10 m Turbulent sensible heat flux	(t)	Meteorological tower	Cox et al. (2023); Cox et al. (2023)
$z_{0,m}$	m	Roughness length for momentum	(t)	Meteorological tower	Cox et al. (2023); Gallagher (2023)
c_CCN	$\mathrm{m^{-3}}$	Cloud condensation nuclei concentration	(t)	ARM optical particle counter	Koontz et al. (2020)
c_INP	$\mathrm{m^{-3}}$	Ice nucleating particle concentration	(t)	DRUM aerosol sampler	Creamean (2022)

ing particles. However, these limits do not apply to the secondary production of ice. It is worth noting that developing an accurate microphysics scheme for the Arctic is a highly researched topic (Fridlind et al., 2012; Ong et al., 2022) that cannot be covered within the scope of this study, but by including the mentioned changes, realistic ice production has been achieved.

2.2.3 Radiation

By default, *DALES* uses a four-stream solver based on (Fu & Liou, 1993; Liou et al., 1988) in combination with Monte Carlo Spectral Integration (Pincus & Stevens, 2009) to calculate the vertical component of the radiative fluxes in the short- and longwave. Previously, the optical properties of ice water content in the radiation calculation were estimated to be identical to a liquid water content of the same mass and a prescribed constant number concentration. While this was expected to introduce an inevitable error in general, it proved to be an unusable assumption for thin ice clouds in the Arctic. For this work, the description of the optical properties of ice crystals followed Fu and Liou (1993). This parameterization was developed for cirrus ice clouds with effective ice diameter in the range $20 - 120\,\mu\text{m}$.

Prior to this study the *DALES* code had never been applied to central Arctic conditions. A necessary step was to supply the radiation scheme with realistic information about the effective diameter of ice crystals. These are here based on the physical properties of ice crystals (McFarquhar & Heymsfield, 1998; Baran, 2005), as estimated from the microphysics scheme. How microphysical properties of ice crystals such as size, geometry, and density can be linked to radiative properties is not yet fully understood, and is an active research topic (Ryan, 2000; Mitchell, 2002; Konoshonkin et al., 2017; Ham et al., 2017). For this reason, the mean particle diameter calculated by the microphysics bulk scheme is for simplicity directly used as the radiative effective diameter. This simplification should be kept in mind when interpreting the results presented in this study. Testing more complex models for the effective diameter of ice particles in the LES is for now considered a future research topic.

Finally, two further simplifications in the treatment of radiation should be mentioned. Firstly, in grid boxes with a mean ice crystal size outside of the range defined above, the effective diameter is set to the upper (respectively lower) bound. Secondly, the solar zenith angle is set constant for the duration of each simulation, and is calculated based on the location and time of the radiosonde used for initialization of the model. The zenith angle affects the solar radiation, but three-dimensional effects are not considered, and radiative transfer works purely in the vertical.

2.2.4 Surface parameterization

The parameterization of surface processes, particularly flux calculations, becomes necessary when using *DALES* due to the unresolved surface-roughness scale. Assuming that the first model level lies in the atmospheric surface layer, computing the exchange between atmosphere and surface becomes possible based on the Monin-Obukhov theory and the surface layer bulk Richardson number Ri_B (Louis, 1979):

$$Ri_\mathrm{B} = \frac{z_1}{L} \frac{\left[\ln\frac{z_1}{z_{0,\mathrm{h}}} - \Psi_\mathrm{H}\left(\frac{z_1}{L}\right) + \Psi_\mathrm{H}\left(\frac{z_{0,\mathrm{h}}}{L}\right)\right]}{\left[\ln\frac{z_1}{z_{0,\mathrm{m}}} - \Psi_\mathrm{M}\left(\frac{z_1}{L}\right) + \Psi_\mathrm{M}\left(\frac{z_{0,\mathrm{m}}}{L}\right)\right]^2}. \tag{1}$$

Here, z_1 is the height of the first model level, L the Obukhov length, $z_{0,\mathrm{h}}$ and $z_{0,\mathrm{m}}$ the roughness lengths for heat and momentum, respectively, and Ψ_H and Ψ_M the integrated stability functions. For a more detailed description refer to Heus et al. (2010).

The stability functions for the unstable and neutral conditions are unchanged from the initially released code base, while for the stable conditions, the stability functions by Grachev et al. (2007) are newly implemented. They were specifically developed for the Arctic regime based on data from the SHEBA campaign suiting this application. The use of roughness lengths derived from *MOSAiC* measurements is discussed in section 2.3.4.

Originally, the computation of sensible and latent heat fluxes at the surface relied on a single uniform surface skin temperature. However, a slightly different approach was introduced, which considers two distinct skin temperatures: the ice skin temperature measured and the ocean skin temperature set to $t_{\mathrm{skin,ocean}} = -1.8\,^{\circ}\mathrm{C}$. By computing fluxes for both temperatures and then taking a weighted average based on the sea-ice fraction, this approach allows for partial inclusion of open ice effects into the simulation. If the ice temperature exceeded $-1.8\,^{\circ}\mathrm{C}$, ocean and sea-ice temperature were assumed to be identical.

The ice skin temperature is prescribed and constant throughout the simulation. This one-way surface-atmosphere coupling reduces the complexity of the simulation immensely, and the error it introduces is expected to be minimal, primarily because of relatively short simulation times.

2.3 Experimental configuration

2.3.1 Domain and grid

The choice of domain and grid size is crucial for the quality of a simulation. The adopted spatial discretization reflects the limits computational resources impose on simulating a full year at turbulence-resolving resolutions. Ensuring that turbulent structures are accurately represented is imperative, which requires a sufficient grid resolution. To avoid the unwanted effects of periodic boundaries in the horizontal directions, the domain must be appropriately sized to provide mesoscale structures with enough space to evolve. In the standardized setup, the horizontal domain and grid utilized are:

$$L_x = L_y = 6400\,\mathrm{m}$$
$$\Delta x = \Delta y = 20\,\mathrm{m}$$

An Eulerian framework is adopted, with the domain fixed in space at the *Polarstern* location. This choice is motivated by our double objective of i) performing short-range simulations lasting only a few hours and ii) being able to compare model results to stationary measurements.

The top of the vertical domain is at $L_z \approx 12\,\mathrm{km}$. The lowest 1200 m of the field is resolved with a grid spacing of $\Delta z_{\mathrm{min}} = 10\,\mathrm{m}$. Above this level, the grid spacing increases exponentially with height until a maximum grid spacing of $\Delta z_{\mathrm{max}} = 185\,\mathrm{m}$. The non-regular vertical grid allows for high resolution in the cloud-containing boundary layer while also accommodating tropospheric features such as higher-level clouds that primarily exert radiative effects on the lower domain. In total, the grid consists of 286 vertical levels. For a more detailed description refer to Appendix A

In the process of finding a compromise between domain size and resolution with fixed available computational resources, it was decided to prioritize resolution: The $6.4\,\mathrm{km} \times 6.4\,\mathrm{km}$ domain is enough to allow for thermodynamic heterogeneities in the virtual area but might lack the evolution of larger mesoscale structures. Since this work is focused on accurately representing realistic conditions and smaller-scale processes in the Arctic atmospheric boundary layer, the resolution that has been selected is satisfactory. The small grid boxes, especially in the lowest layers, enable an accurate representation of turbulence and all turbulence-driven processes, e.g., cloud evolution and life cycle, entrainment, shear-layer mixing, detailed distribution of microphysical interactions, surface fluxes, etc. This setup is referred to as PRODUCTION setup in the following.

A second configuration (TEST) was employed: By reducing the horizontal domain to $800\,\mathrm{m} \times 800\,\mathrm{m}$ and the horizontal resolution to $25\,\mathrm{m} \times 25\,\mathrm{m}$ the computational expense is reduced drastically. The vertical grid is kept unchanged. While this resolution and domain size decrease the simulation quality, the results are still greatly informative. The TEST configuration proved to be crucial in curating and testing the standardized setup and the integration of measurements in an efficient manner. This procedure of using micro-grids to inform the setup of expensive runs was inspired by Neggers, Chylik, et al. (2019). Table 2 summarizes the two setups.

Table 2. Resolution and domain size for different setups.

Setup	Resolution (h × v)	Domain (h × v)	Usage
PRODUCTION	$20\,\mathrm{m} \times (10 - 185\,\mathrm{m})$	$6.4\,\mathrm{km} \times 12\,\mathrm{km}$	Definitive runs
TEST	$25\,\mathrm{m} \times (10 - 185\,\mathrm{m})$	$0.8\,\mathrm{km} \times 12\,\mathrm{km}$	Impact studies

2.3.2 Initial profiles

The initial conditions of each simulation are mostly derived from data gathered during the *MOSAiC* campaign to constrain the experiments as much as possible with measurements. All initial profiles, most of which concern prognostic variables in the model, are horizontally homogeneous in the simulation domain.

Initial profiles of the two prognostic thermodynamical state variables in *DALES*, total water specific humidity q_t and liquid water potential temperature θ_l, are derived from data from the 11:00 UTC radiosonde launched at the *Polarstern* (Maturilli et al., 2022). Corrections were applied to account for elevated launch height and initial sensor adjustment after launch by Dahlke et al. (2023). For this purpose, the radiosonde data was combined with measurements from the *MetCity* meteorological tower (Cox et al., 2023). The prognostic model variables q_t and θ_l in the *DALES* code are derived from the radiosonde temperature, humidity, and pressure measurements. Further, for ice layers, the derived q_v profile was bounded by the saturation specific humidity $q_\mathrm{sat,i}$, to limit the impact of measurement uncertainties on the sensitive initialization of ice clouds. The full procedure is detailed in Appendix B.

The two prognostic variables of suspended cloud mass, cloud liquid water content (LWC) and ice water content (IWC), are also initialized with measurement-based profiles. In the *DALES* code, these variables are denoted as q_l and q_i, respectively. Initializing cloud variables with observations reflects our objective of simulating and resolving small-scale turbulent variability around the *MOSAiC* instrumentation, which is often driven by cloud processes. One could initialize with a cloud-free state and let mixed-phase clouds develop by themselves over time. However, previous LES intercomparison studies on mixed-phase clouds have shown that this is difficult to achieve in a short simulation time (Neggers, Chylik, et al., 2019; Stevens et al., 2018), and the simulations tend to drift significantly away from the initialized atmospheric thermodynamic state as the clouds form. These points motivated the adoption of direct initialization of cloud mass. To achieve this, accurate placement and phasing of the initial cloud mass relative to the vertical atmospheric thermodynamic profile is imperative. Because cloud mass is not directly measured by the radiosonde, the data product of Shupe et al. (2015) is used in this study. The multi-sensor cloud retrieval product features vertically resolved LWC and IWC at 1 min resolution. To ensure that extreme values are avoided and the overall thermodynamic state of the boundary layer is captured, the initial conditions used are mean LWC and IWC profiles. This approach focuses on representing the average conditions across the entire domain rather than the potential heterogeneities in certain areas. In each case, the 1 min profiles from the data set are averaged for 15 min after the radiosonde launch time, around 11:00 UTC, depending on the day. This time window is sufficient to average across individual cloud-turbulence elements yet brief enough to prevent alterations in the overall large-scale atmospheric conditions.

The prognostic humidity budget equation in *DALES* is formulated in terms of $q_\mathrm{t} = q_\mathrm{v}+q_\mathrm{l}$ as the total humidity and excludes suspended cloud ice which is treated as a separate prognostic variable. To achieve an internally consistent initialization of all humidity state variables, q_v, q_l, and q_i are combined in a height-dependent way, as follows. In areas of expected turbulent ice production (below z_{cut}, see equation (B7)), the ice and liquid water specific mixing ratio are added and given to the model as only liquid. The expected behavior of the model is to convert the additional liquid into ice via the microphysics scheme and represent accurate IWC and LWC distributions after a spin-up phase. In areas of expected deposition ice production (above z_{cut}), the retrieved IWC is directly included in the model. If ice is measured, the model will place ice clouds directly with an estimated effective radius of 55 µm. This shortens the lengthy deposition spin-up process and produces realistic, weakly turbulent, high-level ice clouds.

The initial profile of the cloud condensation nuclei (CCN) concentration in the *DALES* mixed-phase microphysics scheme (see 2.2.2) are estimated based on the observations from the *Cloud Condensation Nuclei Particle Counter* located aboard *Polarstern* (Koontz et al., 2020). The measurements show high seasonal and day-to-day variability, as well as variability during some days. However, with an emphasis on the consistency of the setup, the mean value of each day is used as the initial value of CCN concentration for the simulation. The value from the preceding recorded day was used for days missing data. In the absence of a consistent CCN profiling of the Arctic air, the measurements in the bottom part of the atmosphere are considered a good proxy for the conditions in the rest of the boundary layer.

The number concentration of activated ice nucleating particles (INP) is not yet treated prognostically in the current version of the *DALES* microphysics scheme. In the code, the INP concentrations are determined from temperature-dependent activation spectra (Seifert & Beheng, 2006), prescribed by exponential functions with constant parameters proposed by Reisner et al. (1998). Laboratory measurements of INP activation from in-situ samples of Arctic air extracted near *Polarstern* during *MOSAiC* (Creamean et al., 2018; Creamean, 2022) showed a high time-variation in activation spectra, motivating initialization with daily observed values. The associated observed INP number concentrations were significantly lower than the values proposed by the parameterization mentioned above, often by more than two orders of magnitude. To keep the simulations as representative as possible of the observed atmosphere, the measured activation spectra were used instead. A logarithmic regression was applied to each measured spectra from the laboratory samples, and the resulting slope and intercept parameters were then inserted as new values in the deposition-nucleation scheme instead of the original constant values. Finally, limitations in the sampling of the spectra during the drift necessitate adopting two further simplifications in the initialization of the INP profile in the model. Firstly, due to the three-day sampling rate, the spectra on sampling-free days are set at the values from the last preceding day of availability. Secondly, due to the absence of consistent and continuous INP profiling during the drift, the activation spectra are simply assumed constant with height.

2.3.3 Lower boundary conditions

Similar to the initial profiles, the lower boundary conditions for model variables are mainly based on *MOSAiC* data. Additional information is taken from the ERA5 reanalysis. The boundary conditions are prescribed, constant in time, and horizontally homogeneous in the simulated domain.

The sea-ice fraction at the location of the *Polarstern* is taken from ERA5 reanalysis data. With the research vessel frozen in solid pack ice for most of the simulated days, the sea-ice fraction at the ship was often close to 100 %. Accordingly, short-time reductions in the sea-ice fraction, for example, due to lead events, are not considered in the control experiments for simplicity but could simply be added in future sensitivity experiments.

As described in section 2.2.4, two surface skin temperatures are considered in the *DALES* bulk surface parameterization; one for sea ice and one for open water. For the ice surface skin temperature T_{seaice} the brightness temperature measurements at the *MetC-*

ity installation are used (Cox et al., 2023). For the skin temperature of open water, the ocean temperature is used, which is assumed to follow

$$T_{\mathrm{ocean}} = \max\left(T_{\mathrm{seaice}}, -1.8\,^{\circ}\mathrm{C}\right), \tag{2}$$

where the numeric value represents the typical freezing temperature of ocean water. In practice, and for consistency with the profile initialization described above, for T_{seaice} the surface value of the combined data product by Dahlke et al. (2023) is used. This value is the skin temperature measured at *MetCity*. Preliminary experiments demonstrated that the skin temperature is a crucial boundary condition to get right, as it directly determines the upward longwave radiation and strongly affects the low-level stability in the simulations. For this reason, no simulations were carried out for days on which *MetCity* data were not available. Using *ERA5* values as a replacement was no option for these days because i) this would introduce inconsistencies in the boundary conditions during the drift, and ii) warm biases are known to exist in the reanalysis regarding the surface skin temperature (Day et al., 2020). As a guiding principle, integrating different data sets in the simulation for the same quantity goes against the approach of a standardized setup.

2.3.4 Surface properties

The surface roughness length for momentum $z_{0,\mathrm{m}}$ plays a key role in the Monin-Obukhov theory for calculating turbulent fluxes. Accordingly, adopting realistic values is important to get the flux boundary condition right. However, in many model applications, including LES research, the surface roughness length is simply estimated, e.g., ECMWF (2021); Michaelis et al. (2020). Fortunately, $z_{0,\mathrm{m}}$ can be derived from daily *MOSAiC* data of the near-surface wind, turbulence, and temperature measurements (Cox et al., 2023; Gallagher, 2023). This data provides an accurate boundary condition for $z_{0,\mathrm{m}}$ for each simulated day. In the literature the surface roughness length for heat $z_{0,\mathrm{h}}$ in the Arctic is often assumed as $z_{0,\mathrm{h}} = 0.1 \cdot z_{0,\mathrm{m}}$ (e.g. IFS Model ECMWF (2021); Michaelis et al. (2020)). For lack of direct measurements of $z_{0,\mathrm{h}}$ during the drift, this value is also adopted here for the control experiments.

The final boundary condition to be considered concerns the surface albedo α. During polar day, the reflectivity of the predominantly frozen surface directly controls the solar contribution to the surface energy budget. The horizontal scale that α represents is set by the horizontal dimension of the simulated domain. Landscape features such as melt ponds and leads are known to affect the average reflectivity of an area on a meter to kilometer scale (Niehaus et al., 2023), while Arctic weather also influences surface properties on much larger scales. To capture both effects at once, the satellite α product described by Spreen et al. (2008); Istomina et al. (2020) is adopted here. Two main issues affect the accuracy of the satellite estimates of surface albedo; cloud cover and limited satellite overpasses. As a result, satellite albedo products often have significant spatial and temporal gaps. To address this, a rolling average over a week-long period is used to smooth out as many inconsistencies as possible in the data. Secondly, spatial interpolation in the resulting maps gives a reasonable estimate of the albedo in areas around *Polarstern*. It is possible, that the interpolation in time and space introduces an albedo bias toward cloud-free conditions. A further improvement was not considered for two reasons. Albedo measurements for cloudy conditions would be derived from a second dataset, which clashes with the standardized setup. Secondly, the uncertainty by this bias is expected to be small when used in the simplified radiation scheme employed in *DALES*.

2.3.5 Large-scale forcing and nudging

The simulated portion of the atmosphere is not isolated from the larger-scale flow in which it is embedded. Various larger-scale processes impact the development of the atmospheric boundary layer, including large-scale advection, vertical motion, and pressure gradients. In *DALES*, these forcings are considered and applied in a horizontally uniform way, while maintaining height-dependency. The associated tendencies are either fully prescribed or partially interactive with the domain-average profile. This forcing method is described in detail by van Laar et al. (2019) and is, in principle, adopted here, with a few notable exceptions as described below.

In the prognostic budget equations for $\varphi \in \{q_\mathrm{t}, \theta_\mathrm{l}, u, v\}$ the tendency due to large-scale subsidence S_φ^subs is constructed using a prescribed large scale vertical motion w_s and the local vertical gradient, calculated from the vertical profile of the domain averaged variable $\overline{\varphi}$,

$$S_\varphi^\mathrm{subs} = -w_\mathrm{s}\,\frac{\partial \overline{\varphi}}{\partial z} \tag{3}$$

(Siebesma et al., 2003). This means the significant impact of subsidence on inversions is captured. In the momentum equations the pressure gradient (p) and Coriolis (f) forces are represented in combination, through the departure of the actual wind from the geostrophic wind,

$$S_u^\mathrm{p+f} = -f\left(\overline{v} - \overline{v}_g\right), \tag{4}$$
$$S_v^\mathrm{p+f} = f\left(\overline{u} - \overline{u}_g\right), \tag{5}$$

with f the latitude-dependent Coriolis parameter and subscript g indicating the geostrophic state. The latter is calculated from the horizontal pressure fields from ERA5.

In the standardized case generation, the time and location of the *Polarstern* at 11:00 UTC are determined first. Then the six-hour upstream trajectory of the 950 hPa air mass is estimated from the ERA5 reanalysis data. The quantities required for calculating the forcing terms are then calculated at all trajectory points across an area of 1×1 degrees, using the Lagrangian perspective described by Neggers, Chylik, et al. (2019). This means all horizontal advective terms are zero per definition at the height of diagnosis (950 hPa). Finally, the forcing terms are then time-averaged over six hours preceding the arrival of the low-level air mass at the *Polarstern*. This yields time-constant composite forcings, which express how the air mass was modulated by larger-scale processes during the period in which any clouds observed at the *Polarstern* formed. To limit the influence of large-scale processes on the evolution of the simulated domain, horizontal advection of temperature and moisture is set to zero. This approach isolates boundary layer processes as drivers of atmospheric changes.

Continuous Newtonian nudging is applied above the boundary layer thermal inversion to prevent excessive drift of the upper part of the troposphere (Randall & Cripe, 1999; Sobel & Bretherton, 2000; Derbyshire et al., 2004; Neggers et al., 2012). The nudging tendency S_φ^n is formulated in terms of the spatially averaged profiles (Heus et al., 2010; Neggers et al., 2012),

$$S_\varphi^\mathrm{n} = -\,\frac{1}{t^\mathrm{n}}\left(\overline{\varphi} - \varphi^\mathrm{n}\right). \tag{6}$$

Here, $\overline{\varphi}$ is the horizontal mean of an arbitrary scalar, t^n is the nudging time scale, and φ^n is the profile towards which the model profile is relaxed, which in this case is the initial profile based on the corrected 11:00 UTC radiosonde data. The nudging time scale is set to $t^\mathrm{n} = 10\,800\,\mathrm{s}$. It is only applied above the boundary layer height z_i, which is adaptively calculated based on the maximum liquid water potential temperature gradient. This method is well established in the literature, e.g., (Sandu & Stevens, 2011; Zhang et al., 2013; Neggers et al., 2017). Height z_i as used to define the bottom of the nudging layer is defined to be situated in a specified range, as follows:

$$z_i,\ \text{where}\ \left.\frac{\partial \Theta_v}{\partial z}\right|_{z=z_i} = \max\left(\left.\frac{\partial \Theta_v}{\partial z}\right|_z\right),\ z \in [100\,\mathrm{m}, 5000\,\mathrm{m}] \tag{7}$$

This specification is a practical protection against artificially high gradients near the surface and the tropopause inversion.

The final external forcing to be discussed is the radiative forcing at the top of the simulated domain. The downward radiative fluxes at the model ceiling are calculated by including the part of the full radiosonde (initial) profile in the radiative flux calculations that is situated above the ceiling. This way, impacts of the upper atmosphere on both longwave and shortwave radiative transfer are represented as a soft and interactive boundary condition.

3 Results

With the initialization, boundary conditions, and large-scale forcing thus defined, an experimental configuration is obtained with the following key characteristics;

- The simulated domain represents a statistical, homogeneously forced downscaling of the mean atmospheric column as observed daily at 11:00 UTC at the *Polarstern* during *MOSAiC*;
- The recent history of the low-level air mass is represented through Lagrangian forcing;
- Time-composite forcing means the simulations can quasi-equilibrate, depending on the proximity to a balance in the prognostic budget equations;
- Resolved, small-scale boundary layer processes are free to evolve below the thermal inversion;
- Mixed phase clouds are allowed to spin up and interact with radiation, resolved dynamics, and prognostic aerosol.

This model configuration was arrived at after extensive testing on both smaller and larger grids. A three-dimensional volume rendering of a mixed-phase cloud that results from this setup is shown in figure 1 to illustrate that the turbulent dynamics in which these clouds are embedded are resolved to a high degree with this setup. The presentation of the results with this model setup is subdivided into three parts. Section 3.1 provides an overview of the successfully simulated cases during the year-long *MOSAiC* drift. Section 3.2 presents the statistical evaluation of the model output against a year of *MOSAiC* data, and includes a brief initial discussion on data comparability. Section 3.3 focuses in more detail on three selected days, to gain insight into the typical behavior of single simulations and to explore the potential use of the generated library of simulations for further scientific research.

3.1 Simulation overview

Figure 2 gives an overview of the days during the *MOSAiC* drift that were successfully simulated in the PRODUCTION setup featuring the highest resolution and the largest domain, as described in Table 2. Here, success implies two things:

- The data needed for the standardized setup is complete and available at 11:00 UTC;
- No numerical issues occurred, and the simulation was completed successfully.

A subset of non-simulated days can be distinguished that is more or less randomly distributed in time. On these days, typically, an observational dataset is missing that is part of the experimental setup. Two longer, continuous periods also exist that are not simulated; one in May-June 2020 and another in July-August. These coincide with the *Polarstern* not being at the ice floe or *MetCity* not being operational. If not stated otherwise, all results discussed below represent the PRODUCTION setup.

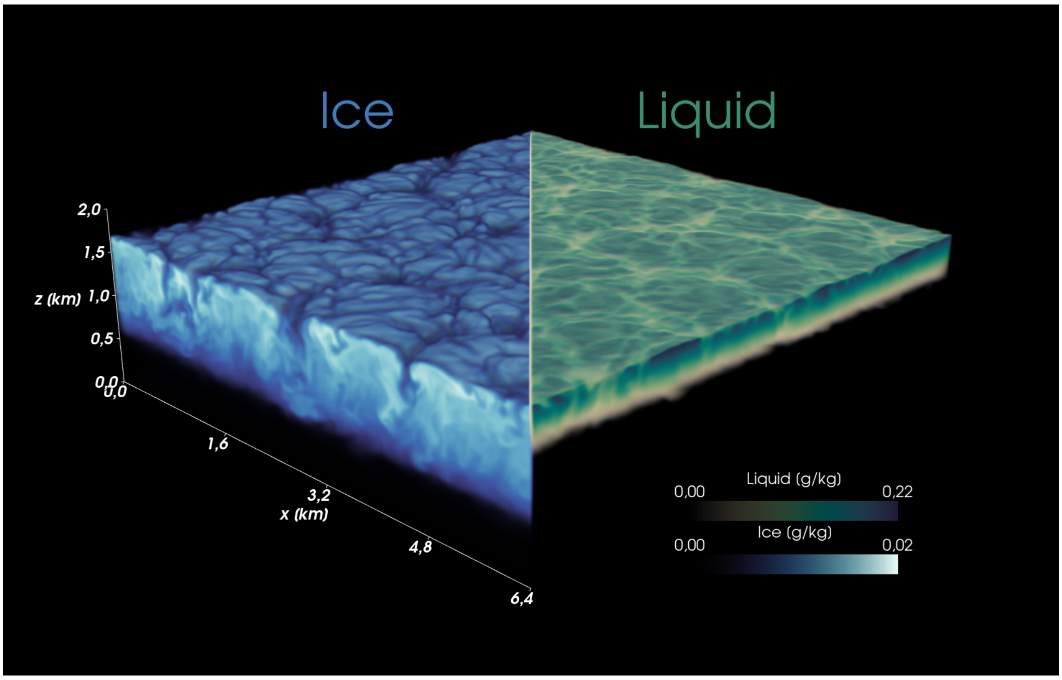

Figure 1. Volume rendering of the *20191101* case (see table 3) after 1.5 h of the full horizontal domain. The two quantities shown are the specific mixing ratios for ice (blue) and liquid (green) water. For visual reasons, the ice is only shown on the left, and the liquid only on the right.

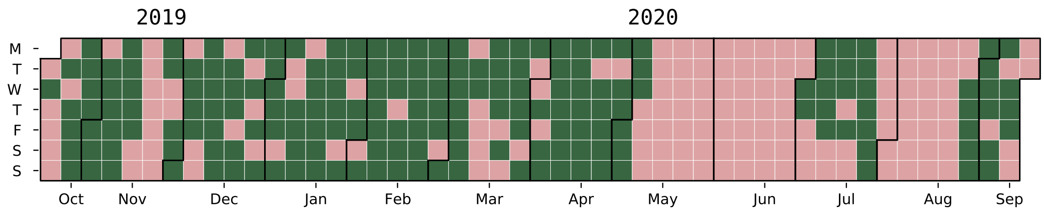

Figure 2. Overview of simulated case studies by date. Green indicates a successful simulation of the state of the boundary around 11:00 UTC at the *Polarstern*. Red shows days on which simulations were unsuccessful.

3.2 Statistical evaluation

The objective of this section is to evaluate the library of daily LES experiments against the year-long record of *MOSAiC* data. The general approach is to assess the difference between simulated values and their measured counterparts for selected variables to identify both strengths and weaknesses of the library of simulations concerning resolved aspects of the Arctic boundary layer and the surface energy budget. When interpreting the simulations and comparing them to measurements, three important considerations should be made, as briefly discussed here.

The first consideration is the *state of equilibrium* of the simulated and observed boundary layer. When the sum of all sources and sinks in the bulk ABL budget is non-zero, a net tendency exists that can gradually warm, cool, moisten, or dry the layer. Due to our lack of knowledge of these tendencies in nature, it remains unknown if the observed ABL is close to equilibrium or not. The simulated ABL can similarly be out of equilibrium, for example, through uncertainties in the applied forcings. However, what helps in model-observation comparability is the well-known slow adjustment of Arctic boundary layers, reflecting that net bulk tendencies are small compared to individual budget terms (Neggers, Chylik, et al., 2019). Another convenient factor is the observed persistence of ABL-related phenomena such as clouds (Shupe et al., 2006; Shupe, 2011; Stramler et al., 2011; Morrison et al., 2012), which implies that the model budget should be pretty similar to the observed one when initializing with observed cloud profiles. For these reasons, it is assumed a priori that the simulated ABL is, in principle, comparable to its observed equivalent. When doing so, one still needs to determine the optimal time point after initialization at which a comparison can be made. On the one hand, turbulent-cloudy processes need to spin up properly; on the other, significant drift from the desired state can happen and needs to be minimized. Careful equilibration analysis of all simulations yielded an optimal time point of 1.5 h after initialization. More details about this analysis can be found in Appendix C.

The second important consideration in the evaluation effort is the *independence of the observational data* from the numerical experiments. What is relevant is that the latter are already closely based on *MOSAiC* datasets. Ideally, one should evaluate resolved processes in the LES against completely independent datasets. This is indeed the case for a large subset of evaluation datasets, such as the surface radiative and turbulent energy fluxes. However, in principle, cloud properties are far less independent from the simulations, as these are initialized with observed cloud profiles. Nonetheless, it should be noted that clouds in the model can significantly evolve during the simulated period before the sampling time point due to strong interactions between thermodynamics, turbulence, and radiation. Accordingly, it is far from trivial that clouds remain unchanged from their initial state. This makes comparison to the observed cloud properties meaningful; a close agreement reflects model skill in maintaining the turbulent cloud layer.

The third consideration is about *uncertainties* in the observational datasets and how to deal with them in the model evaluation. A complicating factor is that these uncertainties also flow into the model setup through the initialization and boundary conditions. How these errors percolate into the final simulation, and to what degree, is hard to disentangle and even harder to isolate from other error sources such as numerics and the prescribed forcings. For these reasons, it was decided to exclude error bars in the evaluation plots. A thorough error analysis is for now considered future work.

3.2.1 Radiative energy fluxes

3.2.1.1 Longwave radiation Figure 3 shows scatter plots of the simulated versus observed near-surface longwave radiative fluxes at the *MetCity* site located on the ice floe near the *Polarstern* (Cox et al., 2023; Riihimaki, 2021). Included are the a) upward, b) downward, and c) net fluxes at 1−3 m height. The simulated upward flux reproduces the observed values to a high degree, in part because the surface skin temperature used in the simulations is derived from these radiation measurements. The good agreement confirms that the radiation scheme accurately represents the radiative energy emitted by the surface. A slight warm bias exists, which is introduced by the use of the double skin temperature as described in Section 2.3.3. The radiation scheme also uses this combined skin temperature (weighted by the sea-ice fraction) as the surface emission temperature for the wider area, while the measured fluxes purely reflect the local temperature of the (colder) sea ice on which they were made.

For the longwave downward flux (that indirectly reflects cloud presence) the agreement is also satisfactory, especially for the upper and lower tails of the distribution (Fig. 3b). This agreement indicates that the model does a reasonable job of simulating both the atmospheric temperature and the vertical location and presence of clouds. In the lower intermediate range, some positive outliers exist. To gain insight, Fig. 4 shows the same data but now shaded according to the (a) ice water path (IWP) and the (b) liquid water path (LWP). This additional information reveals that good agreement exists for i) cold and cloud-free conditions ($LW_{\mathrm{down}} \leq 120\,\mathrm{W\,m^{-2}}$) as well as ii) warm and optically thick liquid clouds ($LW_{\mathrm{down}} \geq 200\,\mathrm{W\,m^{-2}}$). The intermediate range suffers from a well-defined bias for relatively high IWP values, suggesting too high emissivity by thick ice clouds in the model. A deeper investigation of high-bias days revealed that the error is introduced by parametric assumptions in the *DALES* radiation scheme concerning the effective diameter of ice crystals. An effective diameter range of $20-120\,\mu\mathrm{m}$ is applied, which was originally developed for cirrus clouds. Ice crystals in the Arctic can be observed to exceed that value (Shupe et al., 2006). Capping ice diameters at a too-small value leads to the overestimation of the optical thickness of ice clouds. Additionally, it is uncertain if the mean particle radius calculated by the bulk microphysics scheme can be used with proportional ratio 1 as the radiative effective radius in the radiation scheme. These sensitivities are discussed further in section 4.

Combining the upward and downward fluxes yields the net flux (Fig. 3c). The data shows the bimodal distribution typical of the Arctic, which is reproduced to a reasonable degree by the simulations and is explored in more detail in Section 3.2.4. While a general agreement exists with the observations, as expressed by the relatively low bias compared to the mean signal, the error introduced by the biases in the longwave downward radiation for ice clouds now materializes much more pronouncedly. Analysis indicates that the model particularly struggles in situations with optically thin ice clouds, claiming unrealistically low magnitude net radiative fluxes close to $0\,\mathrm{W\,m^{-2}}$.

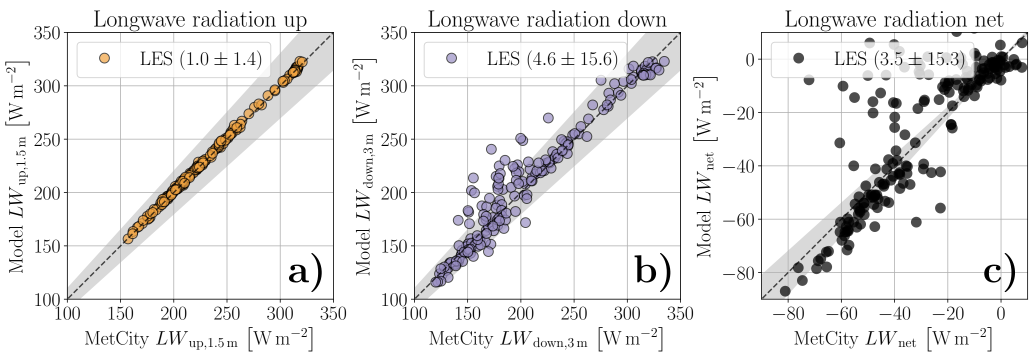

Figure 3. Scatter plots of simulated versus observed a) upward, b) downward, and c) net longwave radiative fluxes. LES results (ordinate) are plotted against *MetCity* tower measurements (abscissa). Each dot represents a single simulated daily case. The simulation is sampled at $t = 1.5\,\mathrm{h}$ after initialization, while the measurement represents the 15 min average after radiosonde launch time. The dashed line indicates the one-to-one diagonal. The gray shading indicates the $\leq$10 % difference area, for reference. Values in the legend show $\mu \pm \sigma$, with μ and σ being the mean and standard deviation of simulated minus measured values, respectively.

3.2.1.2 Shortwave radiation Figure 5 compares the simulated and observed near-surface shortwave radiative fluxes. Non-zero values indicate polar spring and summer and reflect model performance during the melt season. When interpreting these results, it is important to realize that *DALES* only considers purely vertical radiative transfer. This assumption is commonly made in most atmospheric models, including most present-day LES codes, with only a few notable exemptions. However, it is also a significant simplification of reality that excludes three-dimensional radiative effects, which might introduce biases for low solar zenith angles, as are typical of the Arctic during polar day. With this in mind, the model biases in shortwave fluxes are largest at small values and decrease significantly as the shortwave fluxes increase. In terms of energy flux units, the

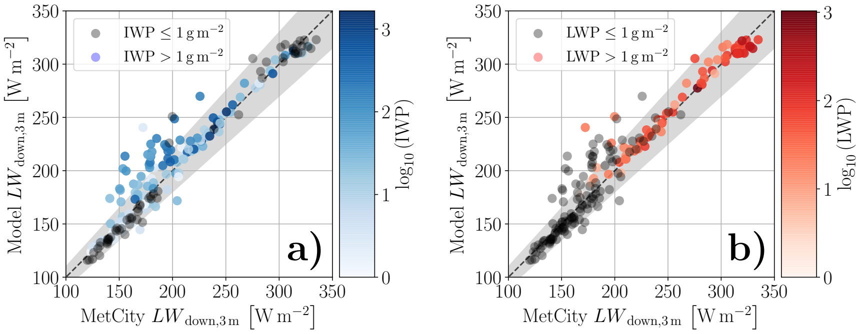

Figure 4. Similar to Fig. 3 b, but now shown with data points color-coded based on the simulated a) ice water path (IWP) and b) liquid water path (LWP).

bias and spread are somewhat larger compared to the longwave fluxes. For all three fluxes, the bias is negative, suggesting that too little shortwave energy is entering the system. This might be due to the exclusion of three-dimensional effects, a hypothesis that needs testing in future research. One notices that the distribution of data points in the upward and downward flux figures is structurally similar. In combination with the accuracy of the upward flux and in association with the resulting net flux, one concludes that the prescribed albedo boundary condition must be close to the true value. This skill was only arrived at after including the satellite-based albedo measurements (not shown).

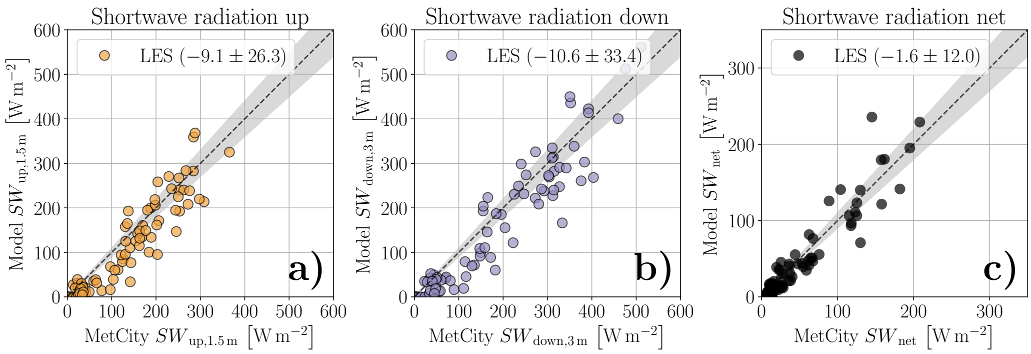

Figure 5. Similar to Fig. 3 but now showing the a) upward, b) downward, and c) net shortwave radiative flux at the surface.

3.2.2 Water paths

Two well-known and critical success metrics for reproducing clouds in the virtual domain are the liquid water path (LWP) and the ice water path (IWP). Figure 6 shows the comparison of simulated and measurement-based values for (a) IWP and (b) LWP. Focusing first on the ice, the general trend of measured IWP is well reproduced by the model. Measurements and model data agree for most cases. Nonetheless, several simulations under- or overestimate the amount of ice in the column. When interpreting these outliers it should be taken into account that the simulations are initialized with the observed profiles of liquid and ice cloud water. Accordingly, in these cases, the offsets arise during the simulated period, which points at the model experiencing difficulties maintaining the right ice amount. Possible causes for this trend include i) lack of resolution to fully resolve cloud-forming dynamical processes in the upper atmosphere, ii) uncertainties in the applied large-scale forcings, and iii) lack of skill in the microphysics scheme. At this point, it is not clear which of these causes apply. However, encouraging aspects are that the model always maintains at least some ice and that the outliers seem randomly scattered around the correct mean as calculated over the full drift.

The measured LWP is mostly well captured by the simulations. A few cases underestimate the amount of liquid. This underestimate can happen when freezing rates are overestimated by the model and liquid clouds glaciate too eagerly. The most significant relative errors for LWP and IWP occur in the region $\leq 50\,\mathrm{g\,m^{-2}}$. Closer inspection of these cases suggested that in situations with really thin ice and liquid clouds, the model is increasingly sensitive to the initial conditions. On the positive side, it can be considered a success that the model can capture and reproduce these thin clouds in the first place, to some degree.

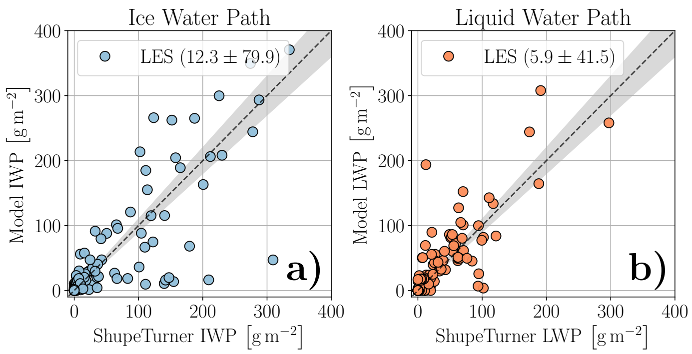

Figure 6. Scatter plot of simulated versus observed a) Liquid Water Path (LWP) and b) Ice Water Path (IWP). The LES is plotted against the ShupeTurner data set. Sampling, notation, and plotting style are analogous to the previous figures.

3.2.3 Near-surface meteorology

Figure 7 shows the simulated versus observed (a) wind speed, (b) temperature, and (c) sensible heat flux at 10 m height. The wind speed in the simulation compares well to the measurements, which is especially gratifying since the wind profile given to each simulation as initial condition stems from *ERA5* reanalysis data. The MOSAiC radiosonde data were assimilated into ERA5. Simulation forcings and near-surface turbulence can cause differences from the initial profile after the spin-up phase. For these reasons, a good agreement is not trivial. Nonetheless, the relative error can be high for low wind speeds, and the impact on near-surface transport processes is significant. The simulation is biased towards lower values for wind speeds $\geq 10\,\mathrm{m\,s^{-1}}$. Low-level jets are a common phenomenon in the high Arctic (López-García et al., 2022), and their underestimation in the LES might explain this small bias.

Figure 7 b shows that the simulated 10 m temperatures closely resemble the observations. This is arguably not surprising, given i) the prescribed observed skin temperature as measured at *MetCity* and ii) the radiosonde temperature profile being part of the model initialization. The close agreement at least confirms that the simulation has not drifted away from the measured thermodynamic state after the spin-up period.

Figure 7 c evaluates the simulated 10 m sensible heat flux (H_s). By convention, a positive sign indicates an upward flux. In general, the observed distribution and orientation of the data points in this space are reproduced, but the mean bias and spread are relatively large compared to the mean signal. The mean bias is negative, expressing a general underestimation of the flux of sensible heat between surface and atmosphere. Significant negative biases occur on individual days, which are responsible for most of the mean bias and spread. On some days, the underestimation reaches more than $20\,\mathrm{W\,m^{-2}}$.

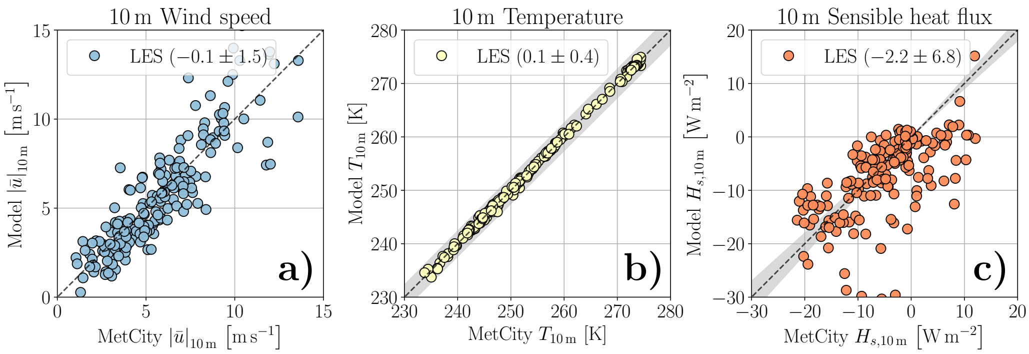

Figure 7. Scatter plots of simulated versus observed meteorological properties at 10 m height, including (a) wind speed, (b) temperature, and (c) bulk sensible heat flux. Sampling, notation, and plotting style are analogous to the previous figures.

The surface H_s is a key player in the SEB, an important aspect of the Arctic climate system, which is crucial to correctly represent in model realizations. Accordingly, it is imperative to gain an understanding of these large differences between the model and measurements. Before claiming model shortcomings, it is relevant to first consider data comparability. At least both the model and observed fluxes rely on bulk methods. The observed fluxes were calculated using the method developed by Fairall et al. (1996), making use of turbulent transfer coefficients and roughness length estimated from the *Surface Heat Budget of the Arctic Ocean* (*SHEBA*) campaign (Andreas et al., 2003). For a more detailed description refer to Cox et al. (2023). As described in Section 2.2.4, the simulations also make use of stability functions based on SHEBA data (Grachev et al., 2007). But the use of roughness lengths based on daily *MOSAiC* measurements in the simulations is a key difference. Adopting the transfer coefficients and roughness lengths improved the simulations from the first attempts in terms of the H_s (not shown). However, potential differences with the SHEBA roughness lengths could explain some of the remaining outlying data points.

More causes can be thought of to explain the differences in the H_s. These include i) local impacts on the measured fluxes not accounted for in the simulations and ii) the possible inapplicability of Monin-Obukhov similarity theory over sea ice in stable wintertime conditions (Heisel & Chamecki, 2023). An interesting alternative data source for comparison with the LES could be the eddy-covariance flux product that is part of the *MOSAiC* data archive (Cox et al., 2023). Further investigating these research questions is for now considered future work. The library of LES experiments presented in this study can inform this effort by providing situations for which large differences occur.

3.2.4 The bimodal Arctic

The surface energy budget of the Arctic is dominated by two primary modes. The first reflects cold, clear, and stable conditions, while the second represents warmer, cloudy states with often neutral or weakly unstable near-surface conditions. This bimodal nature of the Arctic climate system is a long-known phenomenon (Sverdrup, 1933) and has been measured extensively during previous drift campaigns like SHEBA (Persson et al., 1999, 2002; Shupe & Intrieri, 2004; Stramler et al., 2011). The bimodal state has been intensely researched in recent years, given its importance in Arctic Amplification and sea ice melt. In particular, transitions between the dominant modes have been a topic of interest. Previous modeling efforts have contributed to our insight, for example, by linking the bimodality to mixed-phase cloud persistence (Morrison et al., 2012) and large-scale dynamics (Neggers, Chylík, et al., 2019). Also, well-defined bimodality has been used as a metric to test the skill of climate and single-column models (Pithan et al., 2014, 2016; Solomon et al., 2023). Because small-scale dynamics are resolved in LES instead of being parameterized, one expects a priori that the library of *MOSAiC* simulations, as discussed here, should have some skill in reproducing this feature. The availability of 190 realizations under a broad range of atmospheric conditions should provide a sufficient sample size to reproduce the bimodal distribution. These questions are addressed in this section .

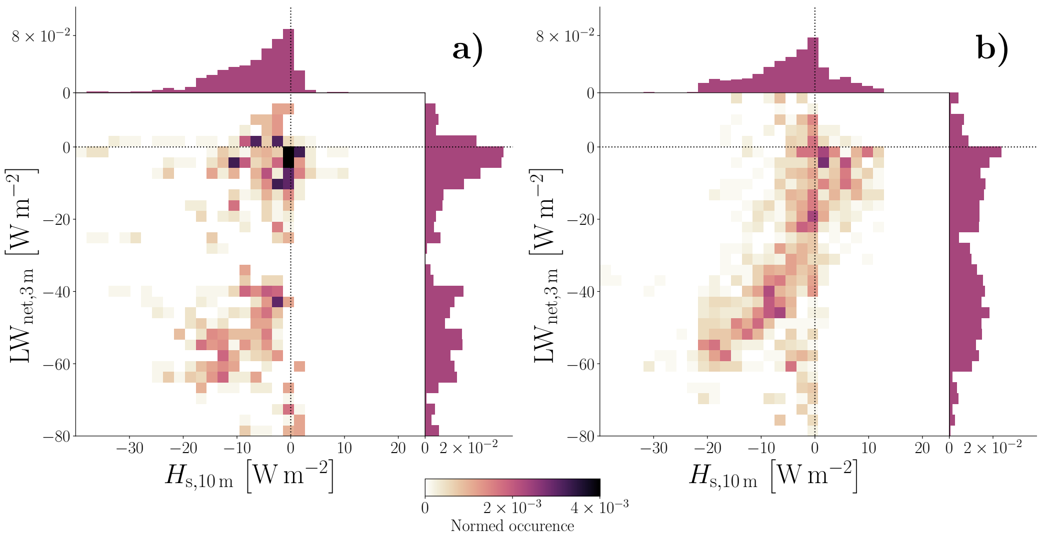

Figure 8. Two-dimensional histograms of normalized occurrence of atmospheric states characterized by the near-surface net longwave radiation (ordinate) and sensible heat flux at 10 m height (abscissa). (a) shows the LES results in which each data point of the given quantities is averaged over 15 min and the whole domain from every simulated case. (b) shows the measured values from *MetCity* (Cox et al. (2023); Fairall et al. (1996), *"bulk_Hs_10m"*) between 10:45 UTC and 11:15 UTC daily.

Figure 8 shows the two-dimensional probability density function (PDF) of near-surface longwave net radiation ($\mathrm{LW_{net}}$) and the near-surface sensible heat flux (H_s), as a) sampled from the year-long library of LES experiments and b) as observed during *MOSAiC*. These two variables were previously discussed individually in Sections 3.2.3 and 3.2.1, respectively, but are combined here. The bimodality is visible in the measurements, with the modes best defined along the $\mathrm{LW_{net}}$ axis. A variety of states is observed between the cloudy mode (near the origin) and the clear mode (bottom left). For convenience, the PDFs are also shown separately as side panels, to better determine and compare the mode locations.

For comparing the model to the measurements the two modes are now considered individually. The cloud-free mode ($LW_\mathrm{net} \leq -30\,\mathrm{W\,m^{-2}}$) is nearly always accompanied by a negative H_s, which can be as low as $-30\,\mathrm{W\,m^{-2}}$ for extremely cold surface conditions. The model correctly reproduces this mode, although the diagonally-shaped maximum is shifted somewhat towards more negative $\mathrm{LW_{net}}$ values. The particularly interesting cluster of cases with extremely low $\mathrm{LW_{net}}$ but near-zero H_s is also well captured by the model. The cloudy state ($LW_\mathrm{net} > -30\,\mathrm{W\,m^{-2}}$) in the LES is situated near the observed one, with a maximum occurrence of $\mathrm{LW_{net}}$ around $0\,\mathrm{W\,m^{-2}}$. However, the LES fails to capture the observed weakly positive H_s occurrences and in general, is biased towards lower heat flux values (as discussed previously in Section 3.2.3). Part of a possible explanation for this underestimation could be the absence of leads in the simulations, which are known to locally boost the sensible and latent heat flux (Li et al., 2020). Additional sensitivity experiments at this location of the phase space could be informative, especially because Cox et al. (2023) note that they are likely to also miss lead effects in their bulk heat flux calculations.

A closer comparison of the simulated and observed $\mathrm{LW_{net}}$ side panels suggests that the LES slightly underestimates the number of intermediate states between the two dominant modes. This is also visible in the two-dimensional phase space. What causes the absence of these intermediate states in the LES is not yet fully understood, and is currently under investigation. Part of the issue could be related to the misrepresentation of longwave radiation emitted by ice clouds discussed in section 3.2.1. More possible causes include the absence of mesoscale variability in the numerical realizations due to spatially homogeneous forcing and small domain size, or an underestimation of cloud-transitional states due to characteristics of the experimental setup.

3.3 Case studies

The statistical evaluation against the full year of data in section 3.2 provides confidence in the basic skill of the LES in reproducing the cloud-radiative climate and surface energy budget of the central Arctic. This section explores a subset of three simulations in more detail. Each simulation serves as a case study of a different Arctic boundary layer, selected to accentuate results of particular interest. Table 3 gives an overview of these cases. The goal is to document resolved boundary-layer processes such as turbulence, and associated features such as vertical structure, inversions, and mixed-phase clouds. This is motivated by the potential use of these virtually resolved data sets in future research efforts.

3.3.1 Vertical structure

Figure 9 shows the potential temperature Θ, the ice q_i, liquid q_l and vapor q_v specific humidity profiles for the three cases. Analogous to previous sections, the simulations are evaluated after 1.5 h run time. The observational data sets served as initial conditions for the simulations. The value of comparing the simulation to its initial conditions is to judge how well the numerical experiment can keep the measured atmosphere in the virtual domain after the spin-up phase.

Table 3. Overview of exemplary case studies shown in section 3.3

Name	Date	Description
20191101	01 November 2019	Single layer mixed-phase cloud
20200216	16 February 2020	Mixed-phase cloud with thin ice cloud above
20200310	10 March 2020	Extremely cold icy atmosphere

The first case simulates the atmosphere measured around the *Polarstern* on November 1, 2019 at 11:00 UTC. Figure 9a-c gives an overview of the results. The boundary layer contains a well-mixed layer decoupled from the surface, as seen from the potential temperature in panel (a). The temperature inversion at 1750 m caps a mixed-phase cloud seen in panel (b). It contains significant mass of liquid at the height 1200−1750 m and a minimal amount of ice at 600 − 1750 m. Here, the mixed-phase cloud is maintained, and the measured liquid and ice water content is reproduced. Only the ice layer around 250 m measured by the ShupeTurner data sets is not found in the simulation. While turbulent processes intensify, the temperature and humidity profile remain nearly unchanged. Only a slight elevation and cooling of the temperature inversion is observed, as expected for a typical Arctic mixed-phase cloud.

The simulation for February 16, 2020 at 11:00 UTC shares several characteristics with the *20191101* case. As seen in figure 9d-f, a decoupled mixed-phase cloud is measured at the *Polarstern* and reproduced by the LES. Additionally, in the spin-up time between the measurement and the evaluation of the simulation, the temperature inversion has lifted slightly while the cloud layer has cooled and water vapor has been depleted. In contrast to the first case, the cloud sits closer to the surface and is topped with a humidity inversion layer around 700 m. A clear success is the ability to maintain this humidity inversion right above the cloud top. The right balance between the entrainment of air above into the cloud layer and cloud-top cooling is crucial in simulating the longevity of mixed-phase clouds. The simulated liquid water profile has a maximum slightly below the cloud top, which is likely a more accurate profile shape than the simple adiabatic profile shape assumed in the observation-based estimate.

The final case discussed simulates March 10, 2020 at 11:00 UTC. It is characterized by an extremely low boundary layer temperature, as can be seen in figure 9g. Further, panel (h) shows a significant amount of ice, especially considering the low amount of total moisture contained in the lower atmosphere (panel (i)). The large amount of ice well-distributed over the column is a typical situation for the Arctic. As discussed in section 2.3.2, ice, that is not expected to be produced by processes in turbulent clouds, is placed in the virtual domain as part of initialization. Despite the assumptions made, this simulation maintains an adequate amount of ice in the atmosphere while also depleting some of the water vapor during the 1.5 h run time. Additional research is needed to evaluate if the model can reproduce accurate freezing rates and precipitation, as these are the main local source and sink processes for ice under extremely cold conditions.

3.3.2 Mixed-phase cloud

In Figure 10 the *20191101* case is shown in more detail. Panel a-c show the same vertical cross-section for the vertical velocity w, and the liquid and ice water specific humidities q_{l} and q_{i}. This is only one of dozens of single-layer mixed-phase clouds simulated in the collection of cases. In comparison to the previous discussion on the averaged vertical profiles, this figure shows the model's capabilities in resolving the smaller-scale dynamics of mixed-phase clouds. The vertical velocity shows the up- and downdrafts in the cloud. Note, that here the downdrafts are stronger in magnitude than the updrafts, since cloud turbulence is mainly driven by cloud-top cooling. This skewness of the vertical velocity distribution is documented in past measurements (Shupe et al., 2013). As seen before, the typical vertical distribution of ice and liquid in mixed-phase clouds is shown: A relatively shallow liquid cloud is the source region for the formation of ice crystals that fall below the liquid cloud base. In this plot, the heterogeneity in the horizontal directions can be observed. There is a visible positive correlation between the vertical velocity and the liquid and ice water. Updrafts supply plentiful moisture to form and grow both cloud liquid and ice, while downdrafts entrain unsaturated air from above into the cloud. A detailed investigation of the interaction between turbulent, thermodynamic, radiative, and microphysical processes in Arctic mixed-phase clouds will be a future topic of research.

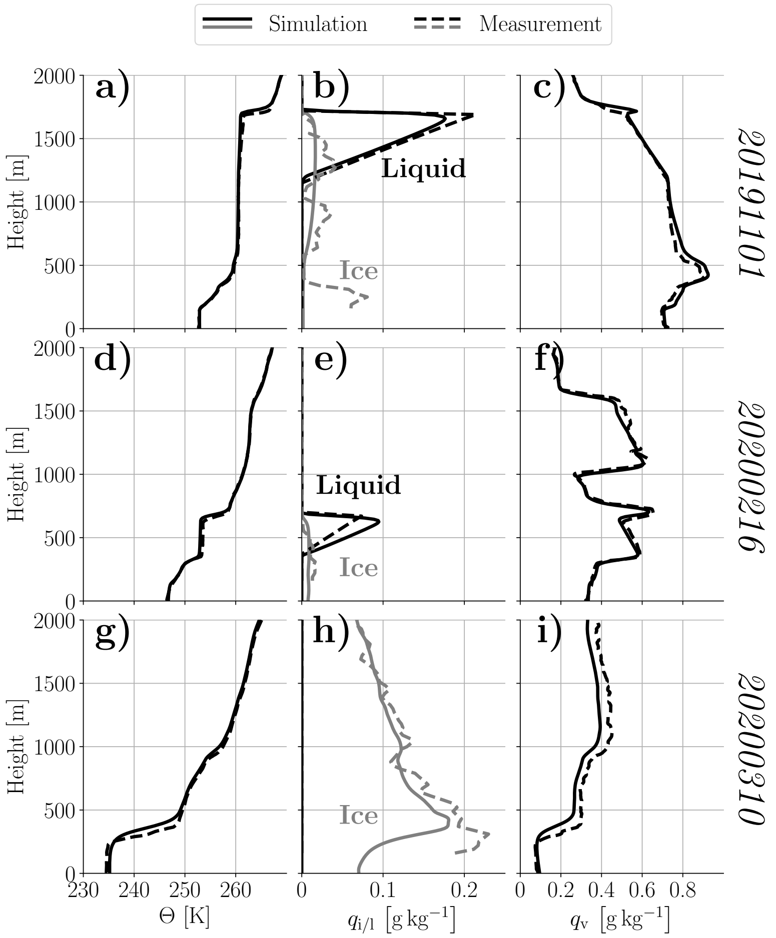

Figure 9. Analysis of the vertical profiles of potential temperature Θ, ice and water specific mixing-ratio $q_{i/l}$, and water vapor specific mixing-ratio q_{v} for the cases *20191101* (a-c), *20200216* (d-f) and *20200310* (g-i). Shown are the simulation results averaged over 15 min in time and over the whole domain in space after 1.5 h run time (solid) and observations at radiosonde launch time around 11:00 UTC (dashed). Observed Θ and q_{v} is derived from radiosonde measurements; $q_{i/l}$ is provided by the ShupeTurner data set.

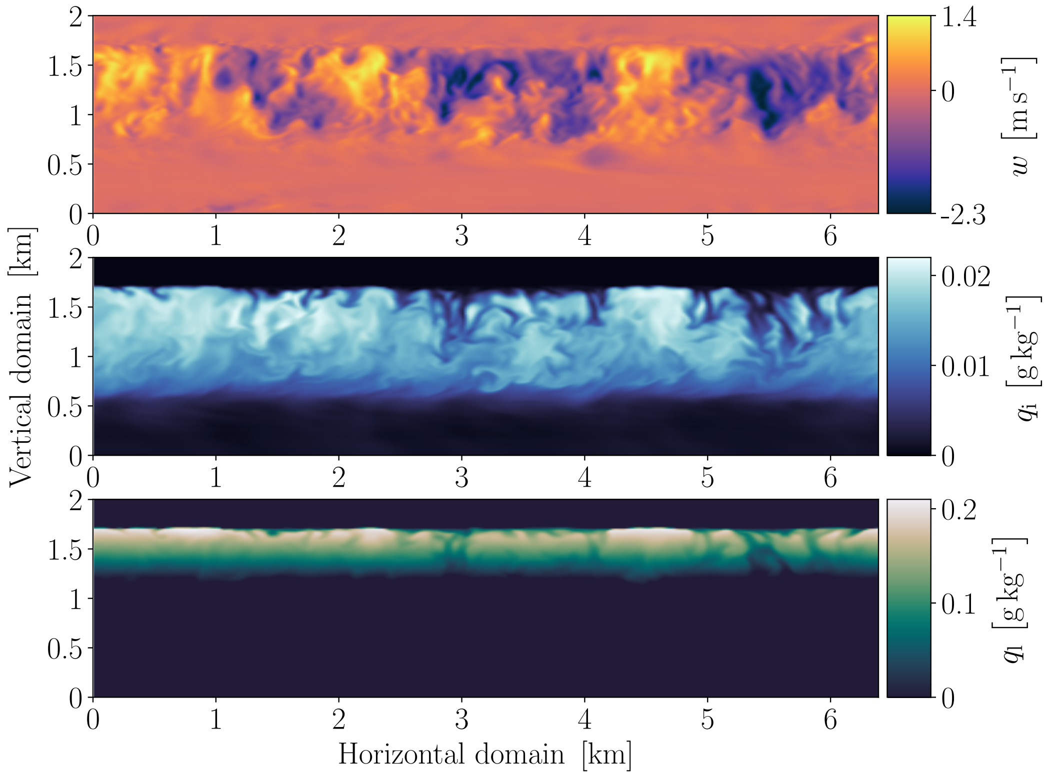

Figure 10. *20191101*: Cross-section plots of vertical velocity w, liquid specific humidity q_l and ice specific humidity q_i. The model output after 1.5 h is shown.

4 Discussion

In the creation of the year-long library of daily LES experiments, some decisions had to be made about the numerical setup, the inclusion of datasets, and the usage of various subgrid-scale parameterizations. All of these decisions affect the eventual results presented and evaluated in the previous section. Gaining insight into these impacts is part of an overarching objective of this study, which is to assess the feasibility of turbulence-resolving LES daily for long continuous periods in the Arctic theatre. To our knowledge, this has not been attempted or achieved before, and can still be considered a "terra incognita" (Wyngaard, 2004). In this section, the impact of various aspects is discussed in more detail to convey this experience to the scientific community and inform possible future efforts of a similar nature.

Grid and domain Existing limitations in computational resources put limits on the feasible domain size, grid size, and spatial resolution of LES. This becomes even more pressing when a high number ($\sim 10^2$) of experiments is to be performed. The first step was to adopt a vertically telescoping grid, as described in Section 2.3.1. For the PRODUCTION runs the horizontal domain size of $6.4\,\text{km}\times6.4\,\text{km}$ was chosen, considered large enough to contain smaller mesoscale features but small enough to allow resolutions sufficient for resolving Arctic turbulence. A key step that proved crucial for arriving at an optimized setup was to use small 32×32 horizontal grid simulations for testing early versions of the model configuration. This was inspired by previous research that adopted a similar strategy for Arctic LES (Neggers, Chylík, et al., 2019). In Figure 11a this TEST setup is compared to the PRODUCTION setup in terms of downward longwave radiative flux. It is evident that the small grid TEST setup, in all its limitations, is still capable of reproducing year-average radiative climate to a high degree. This suggests good enough skill to spin up turbulence and maintain liquid clouds, which are reflected in the longwave flux. The conclusion from this encouraging result is that using small-grid test setups to develop, calibrate, and optimize full LES runs in the Arctic can be effective, not just scientifically but also economically, in terms of reducing computational cost and turnover-time of numerical experiments.

Representation of the surface The representation of the surface significantly affects the simulations. To achieve a workable experimental setup, a few simplifications were made. First, the surface is assumed to be homogeneous, a strong simplification in a region with a notoriously heterogeneous topography (Castellani et al., 2014; Mchedlishvili et al., 2023). The sea ice surface is often covered by snow, acting as an insulator and as a source of blowing ice crystals (Wagner et al., 2022) and a variety of aerosols (Held et al., 2011; Park et al., 2019). While acknowledging these impacts, limitations in data availability on these aspects motivated our decision not to represent them in the control setup. Instead, as a guiding principle, observational data was integrated on only three key surface variables; skin temperature, roughness, and albedo. Open-water effects are included by adapting the skin temperature and humidity to the sea-ice fraction. Figure 11b demonstrates the beneficial impact of integrating the locally observed surface skin temperature as measured at the *MetCity* site instead of using *ERA5* reanalysis data. The in-situ observations are more precise in time and space for the acute situation around the *Polarstern*, and remove most of the spread introduced by the *ERA5* values. Further, the reanalysis values introduce a known well-defined warm bias for colder surface skin temperatures (Herrmannsdörfer et al., 2023). This is evident from the positive shift in emitted longwave radiation for values $\leq 250\,\text{W}\,\text{m}^{-2}$.

Microphysics In early test simulations, the default *DALES* microphysics scheme struggled to maintain liquid and frozen cloud mass for conditions below $-15\,^\circ\text{C}$. A few microphysical processes were found to cause these issues. As described in Section 2.2.2, the parameterization for heterogeneous freezing is not valid for those temperature ranges and had to be limited to the freezing rate for conditions at $-15\,^\circ\text{C}$. In addition, the maximum number concentration for primary ice crystals produced by deposition-nucleation

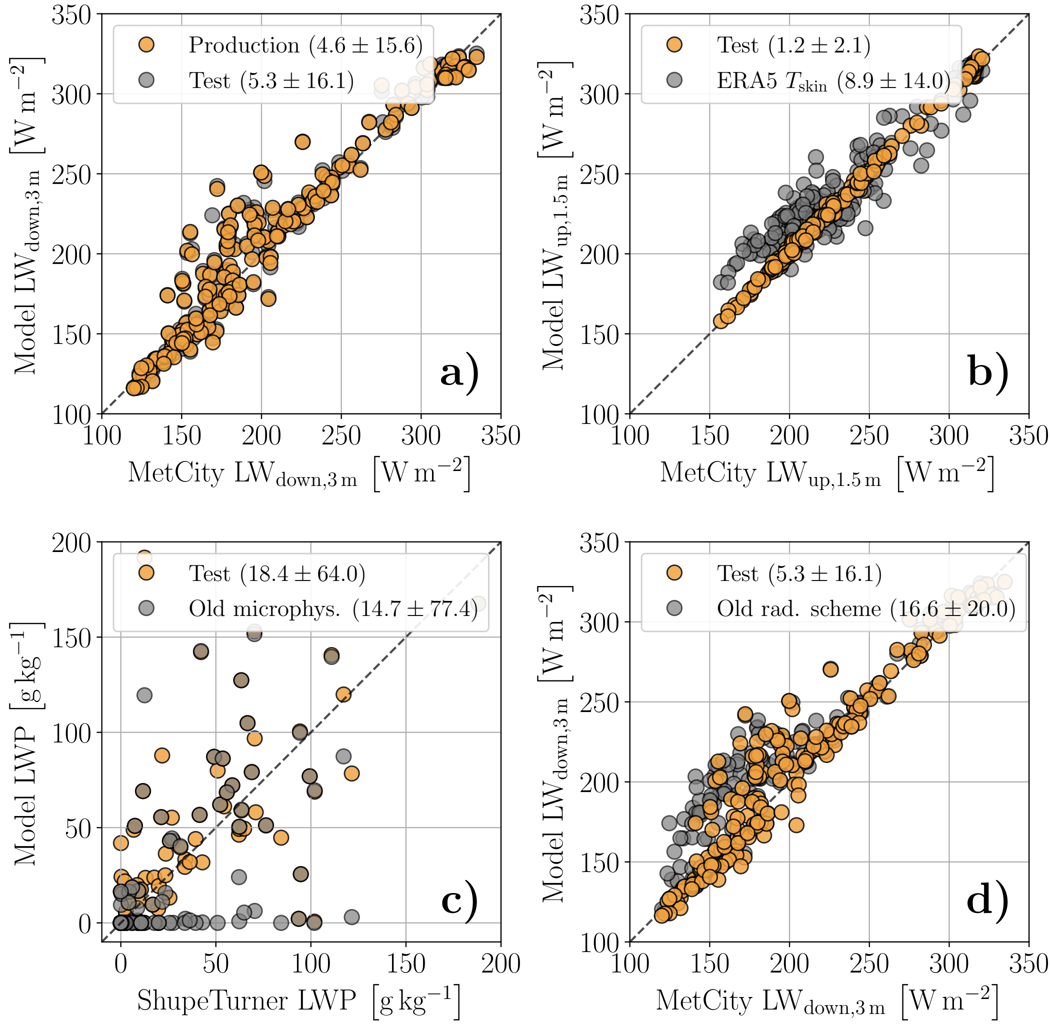

Figure 11. Scatter plots of simulated vs observed variables with different simulation setups. LES results (ordinate) are plotted against *MetCity* (Radiation) or *ShupeTurner* (LWP) measurements (abscissa). Each dot represents a single simulated daily case. The simulations are sampled at $t = 1.5\,\mathrm{h}$ after initialization, the measurements are averaged for 15 min after the radiosonde launch. The dashed line indicates the one-to-one diagonal. Each panel shows the results for two different simulation setups. Panel a) shows the results in downwards longwave radiation for the PRODUCTION and the TEST setup. Analogously, panel b) shows the upwards longwave radiation for the TEST setup and a variation of it with the surface skin temperature derived from *ERA5* data. Panel c) shows the liquid water path for the TEST setup and a variation with the unchanged microphysics scheme. Panel d) shows the downwards longwave radiation for the TEST setup and a variation with the original radiation scheme.

is artificially limited to $200\,\mathrm{L}^{-1}$. Figure 11c shows that under cold conditions, the microphysics scheme in its default setting leads to a full loss of liquid for a significant subset of days, especially for cases with thin ice clouds measured. This loss of liquid stems from an overestimation of the ice production, quickly depleting any liquid contained in the column. Introducing the mentioned fixes in the microphysics scheme enabled realistic simulations of mixed-phase clouds throughout the year, including the Arctic winter.

Ice-radiation interaction Another key step towards a realistic simulation of ice clouds was to separate the treatment of liquid and frozen cloud mass in the radiation scheme. The default *DALES* radiation scheme treated all cloud mass in the same way, a crude simplification that was abandoned for the final set of runs. Figure 11d compares the near-surface longwave downward radiation between the original and adjusted radiation scheme, using the Test setup. Adding separate ice-radiation interaction reduces the mean bias towards higher emissions for colder atmospheres with the default scheme, in particular in the presence of ice clouds, discussed in section 3.2.1. The adjustment does not completely remove the bias. Note, that the cause of this bias seems to stem from exceeding the parameterization limits, but the cause for the large radiative effective radius of the ice crystals might be twofold. Firstly, the ice crystals might be larger than the limits of the radiations scheme (Ryan, 2000), but secondly, the effective radiative diameter of non-spherical ice particles depends on the distribution of particle shapes (Fu & Liou, 1993; Yang & Fu, 2009; Eichler et al., 2009; Mitchell et al., 2011). In 2.2.3 it is assumed that the mean particle radius calculated by the bulk microphysics scheme can be used with proportional ratio 1 as the radiative effective radius in the radiation scheme. The resulting bias in the longwave radiation statistics indicates that this assumption is not fully correct. Improving the approximations of ice-cloud radiation emission and their dependence on the distribution of crystal size and shapes is a goal for future research (Ham et al., 2017; Cairo et al., 2023). These results suggest that the unique impact of ice clouds on radiative transfer can not be ignored, and should be accounted for in model studies of the Arctic climate system. This is in agreement with studies of climate models (Waliser et al., 2011; Fan et al., 2023) that also conclude that further research is required to fully understand and address these shortcomings (Wang et al., 2020).

Other impacts Other aspects of the experimental setup might have a significant impact but are not discussed here for the sake of brevity. These include the treatment of other relevant microphysical processes, aerosol, and the profiles of cloud liquid and ice water content used for model initialization. Investigation of these impacts is ongoing, making use of targeted sensitivity experiments from the library of control runs as described in this study.

5 Summary, Conclusions and Outlook

This study presents a year-long library of daily high-resolution large-eddy simulations (LES) of the atmospheric boundary layer as observed during the recent *MOSAiC* drift campaign in the central Arctic. A specific target is to deeply integrate a multitude of measurements into the experimental configuration. A dedicated standardized model setup for Arctic conditions is developed and employed for this purpose. An overarching science objective is to provide a virtual domain with resolved small-scale turbulence and clouds, which can help in interpreting local measurements made at the *Polarstern* and *MetCity*. To achieve the desired model skill, various sub-grid parameterizations in the LES code for microphysical processes and cloud-radiative interaction had to be adapted to satisfactorily work under central Arctic conditions. The production runs are statistically evaluated against a year of *MOSAiC* data. Three individual case studies are investigated more closely, to assess the model's ability to represent key boundary-layer features including vertical structure and inversions, mixed-phase clouds, and turbulence. The impact of various key aspects of the model and experimental setup is assessed.

The main scientific conclusions coming out of this research can be itemized as follows:

- The statistical evaluation of the library of LES runs demonstrates a generally satisfactory performance under a broad range of meteorological conditions concerning the surface radiative fluxes, the surface sensible heat flux, near-surface meteorology, and mixed-phase clouds.
- The bimodality in the net longwave surface flux typical of the Arctic is well reproduced, with a slight underestimation of intermediate states.
- A weak overestimation of downward longwave radiation under ice clouds is identified, which is traced to artificial parametric limitations on the maximum effective diameter of ice crystals.
- Downward shortwave radiation during polar day is slightly underestimated and speculated to be related to the use of one-dimensional radiative transfer in the model.
- On occasion the surface sensible heat flux, which is an interactive lower boundary condition in the simulations, is underestimated.
- Integrating a multitude of *MOSAiC* data into the initial- and boundary conditions proved crucial for achieving a good statistical agreement. This in particular applies to surface data, sonde data, and value-added cloud products.
- The detailed investigation of three case studies suggests that initialized liquid and ice cloud layers are maintained long enough to survive in the simulations, reflecting that cloud-radiation-turbulence interactions are well captured in this setup.
- Small grid test simulations are shown to be a viable tool for configuring and optimizing full grid LES experiments of Arctic boundary layers.

The obtained results, and the library of high-resolution turbulence-resolving numerical experiments itself, create new research opportunities but also raise some new science questions. An obvious new scientific opportunity is to use the simulations to gain insight into Arctic Amplification at a process level. The three-dimensional model output at high frequencies allows for the sampling of aspects of small-scale physics and dynamics that are still impossible to measure. A prime example relevant for Arctic climate change is the sampling of tendencies of all terms in the energy and water budgets of the Arctic boundary layer and the surface. Targeted perturbation experiments can be conducted to test hypotheses, such as the role of small-scale physical processes in climate feedback mechanisms. The first results of a boundary-layer budget analysis based on the LES dataset for *MOSAiC* as presented in this study was recently published by Linke et al. (2023).

Concerning the LES experiments, the library could still be expanded significantly; only $\sim 25\,\%$ of radiosonde launches were used. Applying the standardized setup to generate more simulations at other sonde launch times is straightforward. While this would represent a significant computational effort, the benefit would be an improved sample size of meteorological conditions throughout the year. The range of observational data sets integrated into the LES experiments could also still be expanded, which might further improve model skills. In addition, for various already integrated datasets alternative products could be used. Assessing the impact of these actions is a future research topic, and could further inform subsequent high-resolution model efforts of a similar nature in the Arctic.

In this study, the model evaluation was limited to a few key *MOSAiC* datasets, selected based on relevance but also on availability for the full drift. More such products are available; in addition, a great number of special measurements are only available for short intensive observation periods. These include tethered balloon data (Lonardi et al., 2022; Akansu et al., 2023; Pilz et al., 2023), unmanned aerial vehicle (UAV) measurements (Egerer et al., 2023; de Boer et al., 2022), among others. The numerical experiments for these periods can play a role in providing context for these observational datasets in terms of small-scale variability surrounding the sites. Conversely, these dedicated special observations can also be used to evaluate the simulations, for example on resolved processes such as turbulence, cloud microphysics, aerosol, and their interactions.

A significant part of the work behind this study went into deriving adequate forcing datasets. The content and format of these daily forcings conform to the input requirements of most single-column models. A good example is the horizontal homogeneity of forcing profiles. With resolved LES results now available to accompany these forcings, and in combination with the extensive *MOSAiC* dataset, this creates a rich testing ground for improving larger-scale weather and climate models in the central Arctic. The option exists to test such models for both the whole drift or for a subset of days, to gain further process-level understanding and inform parameterization improvement.

6 Data availability

One of the key objectives of this work is to make all the created data available. The model code, input, and configuration, the generated forcing files, and the selected model output can be found at doi.org/10.5281/zenodo.10491362. The forcing files are compatible with typical single-column model (SCM) forcings because *DALES* is run with horizontally homogenous initial- and boundary conditions. The standard model output contains extensive data averaged in space and time. Some output is also available as three-dimensional fields. For a more detailed description, please refer to the accompanying documentation. Additional output can always be generated. Please get in touch if needed for your research. Finally, the *DALES* version used for the final runs is 4.3 with an extension for mixed-phase microphysics. The specific version used for this work is uploaded under the link above. For the official *DALES* repository please refer to https://github.com/dalesteam/dales. The combination of forcing files and simulation framework makes the results fully reproducible.

Appendix A Vertical grid

In this section the choice of the vertical grid is detailed. The heights of vertical levels of the grid are calculated as follows:

$$\Delta z^k = \begin{cases} \Delta z_{\text{Start}}, & \text{if } k \leq k_T \\ \Delta z_{\text{Start}} \cdot (1+s)^{k-(k_T+1)}, & \text{if } k_M > k \ > k_T \\ \Delta z_{\text{End}}, & \text{if } k \geq k_M \end{cases}$$

$$z^k = \begin{cases} z^{k-1} + \Delta z^k, & \text{if } k > 1 \\ \dfrac{\Delta z_{\text{Start}}}{2}, & \text{if } k = 0 \end{cases}$$

$$k_T = 120, \quad s = 0.0125, \quad \Delta z_{\text{Start}} = 10\,\text{m},$$
$$k_M = 260, \quad \Delta z_{\text{End}} = 185\,\text{m}$$

This produces a grid with a maximum height of 11 857.23 m. The lower 1.2 km are resolved with a fixed grid spacing of 10 m. From there, the grid spacing expands according to the given formula until it reaches $\Delta z_{\text{max}} = 185\,\text{m}$ at around 7 km height. From there the grid spacing is kept fixed again until the top of the domain. Figure A1 shows the height and grid spacing depending on the grid point.

Appendix B Radiosonde data

The radiosonde variables (Dahlke et al., 2023) used here are the height z, pressure p, temperature T, and the relative humidity RH. From these Θ_v and q_v are calculated

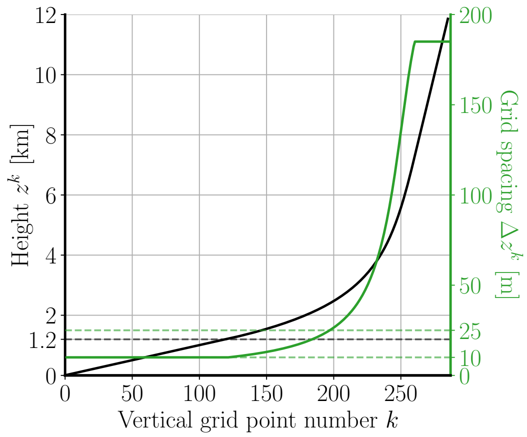

Figure A1. Vertical grid height and spacing of the standardized simulation setup.

using Tetens formula (Tetens, 1930; Murray, 1967):

$$\Theta = T \cdot (p_{\mathrm{ref}}/p)^{R_{\mathrm{d}}/c_{\mathrm{p}}} \tag{B1}$$

$$e_{\mathrm{sat,l}} = e_{\mathrm{sat,0}} \cdot \exp\left[a_{\mathrm{t}} \cdot (T - T_{\mathrm{m}})/(T - b_{\mathrm{t}})\right] \tag{B2}$$

$$q_{\mathrm{sat,l}} = \frac{R_{\mathrm{d}}/R_{\mathrm{v}} \cdot e_{\mathrm{sat,l}}}{p - (1 - R_{\mathrm{d}}/R_{\mathrm{v}}) \cdot e_{\mathrm{sat,l}}} \tag{B3}$$

$$\boxed{q_{\mathrm{v}} = \mathrm{RH} \cdot q_{\mathrm{sat,l}}} \tag{B4}$$

$$\boxed{\Theta_{v} = \Theta \cdot (1 + 0.61 \cdot q_{\mathrm{v}})} \tag{B5}$$

Here, $a_{\mathrm{t}} = 17.27$ (dimensionless) and $b_{\mathrm{t}} = 35.86\,\mathrm{K}$ are dimensionless parameterization constants, $e_{\mathrm{sat,0}} = 610.78\,\mathrm{Pa}$ the reference vapor pressure constant, $R_{\mathrm{d}} = 287.04\,\mathrm{J\,kg^{-1}\,K^{-1}}$ and $R_{\mathrm{v}} = 461.5\,\mathrm{J\,kg^{-1}\,K^{-1}}$ the gas constants for dry air and water vapor, $c_{\mathrm{p}} = 1004\,\mathrm{J\,kg^{-1}\,K^{-1}}$ the specific heat capacity, $T_{\mathrm{m}} = 273.16\,\mathrm{K}$ the melting temperature of ice and $p_{\mathrm{ref}} = 1000\,\mathrm{hPa}$ the reference pressure. Θ is the potential temperature, e_{sat} the saturation water vapor pressure with respect to liquid and q_{sat} the corresponding saturation specific humidity.

A further correction to the derived sonde water vapor specific humidity (q_{v}) profile is made: Thin, high-level ice clouds frequently occur in the Arctic atmosphere - in areas where the air is saturated with water vapor concerning ice. Small measurement uncertainties can lead to situations where $q_{\mathrm{v}} > q_{\mathrm{sat,i}}$ and therefore place unrealistic amounts of cloud ice in the simulation domain. This is prevented by setting

$$q_{\mathrm{v}}(z) = \min\left[q_{\mathrm{sat,i}}(z), q_{\mathrm{v}}(z)\right], \quad \text{for} \quad z \geq z_{\mathrm{cut}} \tag{B6}$$

Here, $q_{\mathrm{sat,i}}$ is the saturation vapor pressure concerning ice calculated analogously to equation (B2) and (B3) with $a_{\mathrm{t,i}} = 21.8746$ and $b_{\mathrm{t,i}} = 7.66\,\mathrm{K}$. The cutoff length z_{cut} is chosen to divide the vertical domain into areas of turbulent ice production in the boundary layer (e.g., in mixed-phase clouds) and areas of deposition ice production. It is calculated as the layer of the highest occurring liquid water content q_{l} above a threshold:

$$z_{\mathrm{cut}} = \max_{z}\left\{z \,\middle|\, q_{\mathrm{l}}(z) \geq 0.01\,\mathrm{g\,kg^{-1}}\right\} \tag{B7}$$

Here, q_{l} is derived as described in section 2.3.2.

Appendix C Evaluation point

To ensure comparability between all cases, a common point in time to evaluate the simulations has to be found. Different issues have to be considered: First, the grand goal of this work is to be able to compare the simulations to *MOSAiC* measurements. The initial conditions are derived once at the start of the simulation and, besides weak nudging, do not influence the further evolution of the atmosphere in the virtual domain. Naturally, after some time, the conditions will have changed so much due to internal turbulent, radiative, and microphysical processes that there is no value in comparing the LES to the measurements anymore. This motivates an early time point for evaluation. But, it has to be considered that the simulation needs time to "spin up". Initially, all variables in the LES are homogeneously distributed in the horizontal directions. Their vertical distribution and wind lead to turbulent mixing in the domain, ultimately creating a realistic spatial distribution of the prognostic variables.

Quantifying the right point in time, considering both of these issues, is difficult to achieve since the atmospheric state varies strongly from case to case. Figure C1 shows the distribution of the absolute change in total turbulent kinetic energy (TKE) in the collection of cases dependent on time. For better comparison, the values are normalized by the average value in the shown interval. Generally speaking, the spin-up phase is associated with a quick change in TKE, since turbulent processes are still developing. A small change in TKE signifies a period of quasi-equilibrium, where the state of the atmosphere is not shifting significantly. Therefore, the point in time for the evaluation of the simulations is chosen to be 1.5 h, around the general minimum of change in TKE.

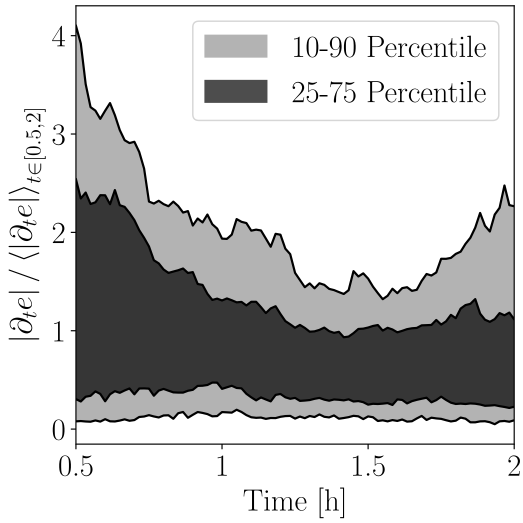

Figure C1. Distribution of normalized absolute change in total turbulent kinetic energy of all simulated cases depending on simulation time.

Acknowledgments

We gratefully acknowledge the funding by the Deutsche Forschungsgemeinschaft (DFG, German Research Foundation) – Projektnummer 268020496 – TRR 172, within the Transregional Collaborative Research Center "ArctiC Amplification: Climate Relevant Atmospheric and SurfaCe Processes, and Feedback Mechanisms $(\mathcal{AC})^3$ ".

Matthew D. Shupe was supported by the NOAA Global Ocean Monitoring and Observing Program (FundRef https://doi.org/10.13039/100018302), the Physical Sciences Laboratory (NA22OAR4320151), and a Mercator Fellowship with $(\mathcal{AC})^3$.

Hersbach et al. (2018a, 2018b) was downloaded from the Copernicus Climate Change Service (C3S) (2023). The results contain modified Copernicus Climate Change Service information 2020. Neither the European Commission nor ECMWF is responsible for any use that may be made of the Copernicus information or data it contains.

We gratefully acknowledge the Gauss Centre for Supercomputing e.V. (www.gauss-centre.eu) for providing computing time on the GCS Supercomputer JUWELS at the Jülich Supercomputing Centre (JSC) under projects VIRTUALLAB and RCONGM.

We furthermore thank the Regional Computing Center of the University of Cologne (RRZK) for providing computing time on the DFG-funded (Funding number: INST 216/512/1FUGG) High-Performance Computing (HPC) system CHEOPS as well as support.

This work used resources of the Deutsches Klimarechenzentrum (DKRZ) granted by its Scientific Steering Committee (WLA) under project ID 1339.

Data used in this manuscript were produced as part of the international Multidisciplinary drifting Observatory for the Study of Arctic Climate (*MOSAiC*) with the tag MOSAiC20192020. We thank all persons involved in the expedition of the Research Vessel Polarstern during MOSAiC (AWI_PS122_00).

Radiation data was obtained from the Atmospheric Radiation Measurement (ARM) User Facility, a U.S. Department of Energy Office of Science User Facility managed by the Biological and Environmental Research Program.

Special thanks go out to Sandro Dahlke for providing early access to enhanced radiosonde data (Dahlke et al., 2023), to Michael Gallagher for the possibility of using an early iteration of surface roughness length measurements (Gallagher, 2023), and to Amy Solomon and Ola Persson for fruitful and insightful discussions, that significantly improved our LES experiments. Finally, we thank Hannes Griesche and Patric Seifert for the conversations about cloud measurements.

References

Akansu, E. F., Dahlke, S., Siebert, H., & Wendisch, M. (2023). Evaluation of methods to determine the surface mixing layer height of the atmospheric boundary layer in the central arctic during polar night and transition to polar day in cloudless and cloudy conditions. *Atmospheric Chemistry and Physics*, *23*(24), 15473–15489. Retrieved from https://acp.copernicus.org/articles/23/15473/2023/ doi: 10.5194/acp-23-15473-2023

Andreas, E. L., Fairall, C. W., Grachev, A. A., Guest, P. S., Horst, T. W., Jordan, R. E., & Persson, P. O. G. (2003). *Turbulent transfer coefficients and roughness lengths over sea ice: The sheba results.* Retrieved from https://ams.confex.com/ams/7POLAR/techprogram/paper_60666.htm

Baran, A. J. (2005). The dependence of cirrus infrared radiative properties on ice crystal geometry and shape of the size-distribution function. *Quarterly Journal of the Royal Meteorological Society*, *131*(607), 1129-1142. Retrieved from https://rmets.onlinelibrary.wiley.com/doi/abs/10.1256/qj.04.91 doi: https://doi.org/10.1256/qj.04.91

Cairo, F., Krämer, M., Afchine, A., Di Donfrancesco, G., Di Liberto, L., Khaykin, S., . . . Borrmann, S. (2023). A comparative analysis of in situ measurements of high-altitude cirrus in the tropics. *Atmospheric Measurement Techniques*, *16*(20), 4899–4925. Retrieved from https://amt.copernicus.org/articles/16/4899/2023/ doi: 10.5194/amt-16-4899-2023

Castellani, G., Lüpkes, C., Hendricks, S., & Gerdes, R. (2014). Variability of arctic sea-ice topography and its impact on the atmospheric surface drag. *Journal of Geophysical Research: Oceans*, *119*(10), 6743-6762. Retrieved from https://agupubs.onlinelibrary.wiley.com/doi/abs/10.1002/2013JC009712 doi: https://doi.org/10.1002/2013JC009712

Chylik, J., Chechin, D., Dupuy, R., Kulla, B. S., Lüpkes, C., Mertes, S., . . . Neggers, R. A. J. (2023). Aerosol impacts on the entrainment efficiency of arctic mixed-phase convection in a simulated air mass over open water. *Atmospheric Chem-*

istry and Physics Discussions, *2023*, 1–42. doi: 10.5194/acp-23-4903-2023

Cox, C., Gallagher, M., Shupe, M., Persson, O., Blomquist, B., Grachev, A., … Uttal, T. (2023). Met City meteorological and surface flux measurements (Level 3 Final), Multidisciplinary Drifting Observatory for the Study of Arctic Climate (MOSAiC), central Arctic, October 2019 - September 2020. *NSF Arctic Data Center*. doi: 10.18739/A2PV6B83F

Cox, C. J., Gallagher, M. R., Shupe, M. D., Persson, P. O. G., Solomon, A., Fairall, C. W., … Uttal, T. (2023). Continuous observations of the surface energy budget and meteorology over the Arctic sea ice during MOSAiC. *Scientific Data*(1), 519. doi: 10.1038/s41597-023-02415-5

Creamean, J. (2022). *Arctic ice nucleation sampling during mosaic.* doi: 10.5439/1798162

Creamean, J. M., Kirpes, R. M., Pratt, K. A., Spada, N. J., Maahn, M., de Boer, G., … China, S. (2018). Marine and terrestrial influences on ice nucleating particles during continuous springtime measurements in an arctic oilfield location. *Atmos. Chem. Phys.*, *18*, 18023–18042. doi: 10.5194/acp-18-18023-2018

Dahlke, S., Shupe, M. D., Cox, C. J., Brooks, I. M., Blomquist, B., & Persson, P. O. G. (2023). *Extended radiosonde profiles 2019/09-2020/10 during MOSAiC Legs PS122/1 - PS122/5* [data set]. PANGAEA. Retrieved from `https://doi.pangaea.de/10.1594/PANGAEA.961881`

Dai, A., Luo, D., Song, M., & Liu, J. (2019, January). Arctic amplification is caused by sea-ice loss under increasing CO2. *Nature Communications*, *10*(1), 121. Retrieved 2023-09-29, from `https://www.nature.com/articles/s41467-018-07954-9` doi: 10.1038/s41467-018-07954-9

Day, J. J., Arduini, G., Sandu, I., Magnusson, L., Beljaars, A., Balsamo, G., … Richardson, D. (2020). Measuring the impact of a new snow model using surface energy budget process relationships. *Journal of Advances in Modeling Earth Systems*, *12*(12), e2020MS002144. Retrieved from `https://agupubs.onlinelibrary.wiley.com/doi/abs/10.1029/2020MS002144` (e2020MS002144 2020MS002144) doi: https://doi.org/10.1029/2020MS002144

de Boer, G., Calmer, R., Jozef, G., Cassano, J. J., Hamilton, J., Lawrence, D., … others (2022). Observing the central arctic atmosphere and surface with university of colorado uncrewed aircraft systems. *Scientific Data*, *9*(1), 439.

Derbyshire, S., Beau, I., Bechtold, P., Grandpeix, J.-Y., Piriou, J.-M., Redelsperger, J.-L., & Soares, P. (2004). Sensitivity of moist convection to environmental humidity. *Quarterly Journal of the Royal Meteorological Society: A journal of the atmospheric sciences, applied meteorology and physical oceanography*, *130*(604), 3055–3079.

de Roode, S. R., Frederikse, T., Siebesma, A. P., Ackerman, A. S., Chylik, J., Field, P. R., … Tomassini, L. (2019). Turbulent transport in the gray zone: A large eddy model intercomparison study of the constrain cold air outbreak case. *J. Adv. Model. Earth Syst.*. (`https://doi.org/10.1029/2018MS001443`) doi: 10.1029/2018MS001443

de Roode, S. R., Sandu, I., van der Dussen, J. J., Ackerman, A. S., Blossey, P., Jarecka, D., … Stevens, B. (2016). Large-eddy simulations of euclipse–gass lagrangian stratocumulus-to-cumulus transitions: Mean state, turbulence, and decoupling. *Journal of the Atmospheric Sciences*, *73*(6), 2485 - 2508. Retrieved from `https://journals.ametsoc.org/view/journals/atsc/73/6/jas-d-15-0215.1.xml` doi: https://doi.org/10.1175/JAS-D-15-0215.1

ECMWF. (2021, 09/2021). Ifs documentation cy47r3 - part iv physical processes. Author. Retrieved from `https://www.ecmwf.int/node/20198` doi: 10.21957/eyrpir4vj

Egerer, U., Cassano, J. J., Shupe, M. D., de Boer, G., Lawrence, D., Doddi, A., … Lonardi, M. (2023). Estimating turbulent energy flux vertical profiles from uncrewed aircraft system measurements: exemplary results for the mosaic campaign. *Atmospheric Measurement Techniques*, *16*(8), 2297–2317. Retrieved from https://amt.copernicus.org/articles/16/2297/2023/ doi: 10.5194/amt-16-2297-2023

Egerer, U., Ehrlich, A., Gottschalk, M., Griesche, H., Neggers, R. A. J., Siebert, H., & Wendisch, M. (2021). Case study of a humidity layer above arctic stratocumulus and potential turbulent coupling with the cloud top. *Atmos. Chem. Phys.*, *21*(8), 6347–6364. Retrieved from https://acp.copernicus.org/articles/21/6347/2021/ (https://doi.org/10.5194/acp-21-6347-2021) doi: 10.5194/acp-21-6347-2021

Eichler, H., Ehrlich, A., Wendisch, M., Mioche, G., Gayet, J.-F., Wirth, M., ... Minikin, A. (2009). Influence of ice crystal shape on retrieval of cirrus optical thickness and effective radius: A case study. *Journal of Geophysical Research: Atmospheres*, *114*(D19). Retrieved from https://agupubs.onlinelibrary.wiley.com/doi/abs/10.1029/2009JD012215 doi: https://doi.org/10.1029/2009JD012215

Fairall, C. W., Bradley, E. F., Rogers, D. P., Edson, J. B., & Young, G. S. (1996). Bulk parameterization of air-sea fluxes for tropical ocean-global atmosphere coupled-ocean atmosphere response experiment. *Journal of Geophysical Research: Oceans*, *101*(C2), 3747-3764. Retrieved from https://agupubs.onlinelibrary.wiley.com/doi/abs/10.1029/95JC03205 doi: https://doi.org/10.1029/95JC03205

Fan, C., Chen, Y.-H., Chen, X., Lin, W., Yang, P., & Huang, X. (2023). A refined understanding of the ice cloud longwave scattering effects in climate model. *Journal of Advances in Modeling Earth Systems*, *15*(10), e2023MS003810. Retrieved from https://agupubs.onlinelibrary.wiley.com/doi/abs/10.1029/2023MS003810 (e2023MS003810 2023MS003810) doi: https://doi.org/10.1029/2023MS003810

Fridlind, A. M., van Diedenhoven, B., Ackerman, A. S., Avramov, A., Mrowiec, A., Morrison, H., ... Shupe, M. D. (2012). A FIRE-ACE/SHEBA case study of mixed-phase arctic boundary layer clouds: Entrainment rate limitations on rapid primary ice nucleation processes. *Journal of the Atmospheric Sciences*, *69*(1), 365 - 389. Retrieved from https://journals.ametsoc.org/view/journals/atsc/69/1/jas-d-11-052.1.xml doi: https://doi.org/10.1175/JAS-D-11-052.1

Fu, Q., & Liou, K. N. (1993). Parameterization of the radiative properties of cirrus clouds. *Journal of Atmospheric Sciences*, *50*(13), 2008 - 2025. Retrieved from https://journals.ametsoc.org/view/journals/atsc/50/13/1520-0469_1993_050_2008_potrpo_2_0_co_2.xml doi: https://doi.org/10.1175/1520-0469(1993)050⟨2008:POTRPO⟩2.0.CO;2

Gallagher, M. (2023). Surface roughness. *Personal corresponence; to be submitted*.

Grachev, A. A., Andreas, E. L., Fairall, C. W., Guest, P. S., & Persson, P. O. G. (2007). Sheba flux–profile relationships in the stable atmospheric boundary layer. *Bound.-Lay. Meteorol.*, *124*(3), 315-333. Retrieved from http://dx.doi.org/10.1007/s10546-007-9177-6 doi: 10.1007/s10546-007-9177-6

Gustafson Jr, W. I., Vogelmann, A. M., Li, Z., Cheng, X., Dumas, K. K., Endo, S., ... Xiao, H. (2020). The large-eddy simulation (les) atmospheric radiation measurement (arm) symbiotic simulation and observation (lasso) activity for continental shallow convection. *Bulletin of the American Meteorological Society*, *101*(4), E462–E479.

Ham, S.-H., Kato, S., & Rose, F. G. (2017). Examining impacts of mass-diameter (m-d) and area-diameter (a-d) relationships of ice particles on retrievals of effective radius and ice water content from radar and lidar measurements. *Journal of Geophysical Research: Atmospheres*, *122*(6), 3396-3420. Retrieved from https://agupubs.onlinelibrary.wiley.com/doi/abs/10.1002/

2016JD025672 doi: https://doi.org/10.1002/2016JD025672

Heisel, M., & Chamecki, M. (2023). Evidence of mixed scaling for mean profile similarity in the stable atmospheric surface layer. *Journal of the Atmospheric Sciences*, *80*(8), 2057 - 2073. Retrieved from https://journals.ametsoc.org/view/journals/atsc/80/8/JAS-D-22-0260.1.xml doi: https://doi.org/10.1175/JAS-D-22-0260.1

Held, A., Brooks, I. M., Leck, C., & Tjernström, M. (2011). On the potential contribution of open lead particle emissions to the central arctic aerosol concentration. *Atmospheric Chemistry and Physics*, *11*(7), 3093–3105. Retrieved from https://acp.copernicus.org/articles/11/3093/2011/ doi: 10.5194/acp-11-3093-2011

Herrmannsdörfer, L., Müller, M., Shupe, M. D., & Rostosky, P. (2023, 02). Surface temperature comparison of the Arctic winter MOSAiC observations, ERA5 reanalysis, and MODIS satellite retrieval. *Elementa: Science of the Anthropocene*, *11*(1), 00085. Retrieved from https://doi.org/10.1525/elementa.2022.00085 doi: 10.1525/elementa.2022.00085

Hersbach, H., Bell, B., Berrisford, P., Biavati, G., Horányi, A., Muñoz Sabater, J., ... Thépaut, J.-N. (2018a). *Era5 hourly data on pressure levels from 1940 to present.* ECMWF.

Hersbach, H., Bell, B., Berrisford, P., Biavati, G., Horányi, A., Muñoz Sabater, J., ... Thépaut, J.-N. (2018b). Era5 hourly data on single levels from 1940 to present. *Copernicus climate change service (c3s) climate data store (cds).*

Hersbach, H., Bell, B., Berrisford, P., Biavati, G., Horányi, A., Muñoz Sabater, J., ... Thépaut, J.-N. (2023). *Era5 hourly data on pressure levels from 1940 to present.* Copernicus Climate Change Service (C3S) Climate Data Store (CDS). doi: https://doi.org/10.24381/cds.bd0915c6

Heus, T., van Heerwaarden, C. C., Jonker, H. J. J., Pier Siebesma, A., Axelsen, S., van den Dries, K., ... Vilà-Guerau de Arellano, J. (2010). Formulation of the dutch atmospheric large-eddy simulation (dales) and overview of its applications. *Geosci. Model Dev.*, *3*(2), 415–444. doi: 10.5194/gmd-3-415-2010

Hundsdorfer, W., Koren, B., vanLoon, M., & Verwer, J. (1995). A positive finite-difference advection scheme. *Journal of Computational Physics*, *117*(1), 35-46. Retrieved from https://www.sciencedirect.com/science/article/pii/S002199918571042X doi: https://doi.org/10.1006/jcph.1995.1042

Istomina, L., Marks, H., Huntemann, M., Heygster, G., & Spreen, G. (2020). Improved cloud detection over sea ice and snow during arctic summer using meris data. *Atmos. Meas. Tech.*, *13*(12), 6459–6472. Retrieved from https://amt.copernicus.org/articles/13/6459/2020/ (https://doi.org/10.5194/amt-13-6459-2020) doi: 10.5194/amt-13-6459-2020

Jenkins, M., & Dai, A. (2021). The impact of sea-ice loss on arctic climate feedbacks and their role for arctic amplification. *Geophysical Research Letters*, *48*(15), e2021GL094599. Retrieved from https://agupubs.onlinelibrary.wiley.com/doi/abs/10.1029/2021GL094599 (e2021GL094599 2021GL094599) doi: https://doi.org/10.1029/2021GL094599

Kiszler, T., Ebell, K., & Schemann, V. (2023). A performance baseline for the representation of clouds and humidity in cloud-resolving ICON-LEM simulations in the arctic. *Journal of Advances in Modeling Earth Systems*, *15*(5), e2022MS003299. Retrieved from https://agupubs.onlinelibrary.wiley.com/doi/abs/10.1029/2022MS003299 (e2022MS003299 2022MS003299) doi: https://doi.org/10.1029/2022MS003299

Klein, S. A., McCoy, R. B., Morrison, H., Ackerman, A. S., Avramov, A., de Boer, G., ... Zhang, G. (2009). Intercomparison of model simulations of mixed-phase clouds observed during the arm mixed-phase arctic cloud experiment. i: single-layer cloud. *Q. J. R. Meteorolog. Soc.*, *135*(641), 979–1002. Retrieved from http://dx.doi.org/10.1002/qj.416 doi: 10.1002/qj.416

Konoshonkin, A., Borovoi, A., Kustova, N., Okamoto, H., Ishimoto, H., Grynko, Y., & Förstner, J. (2017). Light scattering by ice crystals of cirrus clouds: From exact numerical methods to physical-optics approximation. *Journal of Quantitative Spectroscopy and Radiative Transfer*, *195*, 132-140. Retrieved from https://www.sciencedirect.com/science/article/pii/S0022407316305775 (Laser-light and Interactions with Particles 2016) doi: https://doi.org/10.1016/j.jqsrt.2016.12.024
Koontz, A., Uin, J., Andrews, E., Enekwizu, O., Hayes, C., & Salwen, C. (2020). Cloud condensation nuclei particle counter (aosccn2colaavg). *Atmospheric Radiation Measurement (ARM) user facility*. doi: 10.5439/1323894
Li, X., Krueger, S. K., Strong, C., Mace, G. G., & Benson, S. (2020). Midwinter arctic leads form and dissipate low clouds. *Nature Communications*, *11*(1), 206.
Linke, O., Quaas, J., Baumer, F., Becker, S., Chylik, J., Dahlke, S., ... Wendisch, M. (2023). Constraints on simulated past arctic amplification and lapse-rate feedback from observations. *Atmospheric Chemistry and Physics Discussions*, *2023*, 1–37. Retrieved from https://acp.copernicus.org/preprints/acp-2022-836/ doi: 10.5194/acp-2022-836
Liou, K.-N., Fu, Q., & Ackerman, T. P. (1988). A simple formulation of the delta-four-stream approximation for radiative transfer parameterizations. *Journal of Atmospheric Sciences*, *45*(13), 1940 - 1948. Retrieved from https://journals.ametsoc.org/view/journals/atsc/45/13/1520-0469_1988_045_1940_asfotd_2_0_co_2.xml doi: https://doi.org/10.1175/1520-0469(1988)045⟨1940:ASFOTD⟩2.0.CO;2
Lonardi, M., Pilz, C., Akansu, E. F., Dahlke, S., Egerer, U., Ehrlich, A., ... others (2022). Tethered balloon-borne profile measurements of atmospheric properties in the cloudy atmospheric boundary layer over the arctic sea ice during mosaic: Overview and first results. *Elem Sci Anth*, *10*(1), 000120.
Louis, J.-F. (1979). A parametric model of vertical eddy fluxes in the atmosphere. *Boundary-Layer Meteorology*, *17*(2), 187–202.
López-García, V., Neely, I., Ryan R., Dahlke, S., & Brooks, I. M. (2022, 09). Low-level jets over the Arctic Ocean during MOSAiC. *Elementa: Science of the Anthropocene*, *10*(1), 00063. Retrieved from https://doi.org/10.1525/elementa.2022.00063 doi: 10.1525/elementa.2022.00063
Maturilli, M., Sommer, M., Holdridge, D. J., Dahlke, S., Graeser, J., Sommerfeld, A., ... Schulz, A. (2022). *MOSAiC radiosonde data (level 3)* [data set]. PANGAEA. Retrieved from https://doi.org/10.1594/PANGAEA.943870 doi: 10.1594/PANGAEA.943870
McFarquhar, G. M., & Heymsfield, A. J. (1998). The definition and significance of an effective radius for ice clouds. *Journal of the Atmospheric Sciences*, *55*(11), 2039 - 2052. Retrieved from https://journals.ametsoc.org/view/journals/atsc/55/11/1520-0469_1998_055_2039_tdasoa_2.0.co_2.xml doi: 10.1175/1520-0469(1998)055⟨2039:TDASOA⟩2.0.CO;2
Mchedlishvili, A., Lüpkes, C., Petty, A., Tsamados, M., & Spreen, G. (2023). New estimates of pan-arctic sea ice–atmosphere neutral drag coefficients from icesat-2 elevation data. *The Cryosphere*, *17*(9), 4103–4131. Retrieved from https://tc.copernicus.org/articles/17/4103/2023/ doi: 10.5194/tc-17-4103-2023
Michaelis, J., Lüpkes, C., Zhou, X., Gryschka, M., & Gryanik, V. M. (2020). Influence of lead width on the turbulent flow over sea ice leads: Modeling and parametrization. *Journal of Geophysical Research: Atmospheres*, *125*(15), e2019JD031996. Retrieved from https://agupubs.onlinelibrary.wiley.com/doi/abs/10.1029/2019JD031996 (e2019JD031996 10.1029/2019JD031996) doi: https://doi.org/10.1029/2019JD031996
Middlemas, E. A., Kay, J. E., Medeiros, B. M., & Maroon, E. A. (2020). Quantifying the influence of cloud radiative feedbacks on arctic surface warming using

cloud locking in an earth system model. *Geophysical Research Letters*, *47*(15), e2020GL089207. Retrieved from https://agupubs.onlinelibrary.wiley.com/doi/abs/10.1029/2020GL089207 (e2020GL089207 2020GL089207) doi: https://doi.org/10.1029/2020GL089207

Mitchell, D. L. (2002). Effective diameter in radiation transfer: General definition, applications, and limitations. *Journal of the Atmospheric Sciences*, *59*(15), 2330 - 2346. Retrieved from https://journals.ametsoc.org/view/journals/atsc/59/15/1520-0469_2002_059_2330_edirtg_2.0.co_2.xml doi: 10.1175/1520-0469(2002)059⟨2330:EDIRTG⟩2.0.CO;2

Mitchell, D. L., Lawson, R. P., & Baker, B. (2011). Understanding effective diameter and its application to terrestrial radiation in ice clouds. *Atmospheric Chemistry and Physics*, *11*(7), 3417–3429. Retrieved from https://acp.copernicus.org/articles/11/3417/2011/ doi: 10.5194/acp-11-3417-2011

Morrison, H., de Boer, G., Feingold, G., Harrington, J., Shupe, M. D., & Sulia, K. (2012). Resilience of persistent arctic mixed-phase clouds. *Nat. Geosci.*, *5*, 11-17. doi: 10.1038/NGEO1332

Morrison, H., Zuidema, P., Ackerman, A. S., Avramov, A., De Boer, G., Fan, J., ... others (2011). Intercomparison of cloud model simulations of arctic mixed-phase boundary layer clouds observed during sheba/fire-ace. *Journal of Advances in Modeling Earth Systems*, *3*(2).

Murray, F. W. (1967). On the computation of saturation vapor pressure. *Journal of Applied Meteorology and Climatology*, *6*(1), 203 - 204. Retrieved from https://journals.ametsoc.org/view/journals/apme/6/1/1520-0450_1967_006_0203_otcosv_2_0_co_2.xml doi: https://doi.org/10.1175/1520-0450(1967)006⟨0203:OTCOSV⟩2.0.CO;2

Neggers, R. A. J., Ackerman, A. S., Angevine, W. M., Bazile, E., Beau, I., Blossey, P. N., ... Xu, K.-M. (2017). Single-column model simulations of subtropical marine boundary-layer cloud transitions under weakening inversions. *Journal of Advances in Modeling Earth Systems*, *9*(6), 2385-2412. Retrieved from https://agupubs.onlinelibrary.wiley.com/doi/abs/10.1002/2017MS001064 doi: https://doi.org/10.1002/2017MS001064

Neggers, R. A. J., Chylik, J., Egerer, U., Griesche, H., Schemann, V., Seifert, P., ... Macke, A. (2019). Local and remote controls on arctic mixed-layer evolution. *Journal of Advances in Modeling Earth Systems*, *11*(7), 2214-2237. Retrieved from https://agupubs.onlinelibrary.wiley.com/doi/abs/10.1029/2019MS001671 doi: https://doi.org/10.1029/2019MS001671

Neggers, R. A. J., Chylík, J., Egerer, U., Griesche, H., Schemann, V., Seifert, P., ... Macke, A. (2019). Local and remote controls on arctic mixed-layer evolution. *J. Adv. Model. Earth Syst.*, *11*, 2214-2237. (https://doi.org/10.1029/2019MS001671) doi: 10.1029/2019MS001671

Neggers, R. A. J., Siebesma, A. P., & Heus, T. (2012). Continuous single-column model evaluation at a permanent meteorological supersite. *Bull. Am. Meteorol. Soc.*, *93*. doi: 10.1175/BAMS-D-11-00162.1

Nicolaus, M., Perovich, D. K., Spreen, G., Granskog, M. A., Von Albedyll, L., Angelopoulos, M., ... Wendisch, M. (2022, February). Overview of the MOSAiC expedition: Snow and sea ice. *Elem Sci Anth*, *10*(1), 000046. Retrieved 2023-10-10, from https://online.ucpress.edu/elementa/article/10/1/000046/119791/Overview-of-the-MOSAiC-expedition-Snow-and-sea-ice doi: 10.1525/elementa.2021.000046

Niehaus, H., Spreen, G., Birnbaum, G., Istomina, L., Jäkel, E., Linhardt, F., ... Wright, N. (2023). Sea ice melt pond fraction derived from sentinel-2 data: Along the mosaic drift and arctic-wide. *Geophysical Research Letters*, *50*(5), e2022GL102102. Retrieved from https://agupubs.onlinelibrary.wiley.com/doi/abs/10.1029/2022GL102102 (e2022GL102102 2022GL102102) doi: https://doi.org/10.1029/2022GL102102

Ong, C. R., Koike, M., Hashino, T., & Miura, H. (2022). Modeling performance of scale-amps: Simulations of arctic mixed-phase clouds observed during sheba. *Journal of Advances in Modeling Earth Systems*, *14*(6), e2021MS002887. Retrieved from https://agupubs.onlinelibrary.wiley.com/doi/abs/10.1029/2021MS002887 (e2021MS002887 2021MS002887) doi: https://doi.org/10.1029/2021MS002887

Ovchinnikov, M., Ackerman, A. S., Avramov, A., Cheng, A., Fan, J., Fridlind, A. M., ... Sulia, K. (2014). Intercomparison of large-eddy simulations of arctic mixed-phase clouds: Importance of ice size distribution assumptions. *J. Adv. Model. Earth Syst.*, *6*(1), 223-248. doi: 10.1002/2013MS000282

Park, K., Kim, I., Choi, J.-O., Lee, Y., Jung, J., Ha, S.-Y., ... Zhang, M. (2019). Unexpectedly high dimethyl sulfide concentration in high-latitude arctic sea ice melt ponds. *Environ. Sci.: Processes Impacts*, *21*, 1642-1649. Retrieved from http://dx.doi.org/10.1039/C9EM00195F doi: 10.1039/C9EM00195F

Persson, P. O. G., Fairall, C. W., Andreas, E. L., Guest, P. S., & Perovich, D. K. (2002). Measurements near the atmospheric surface flux group tower at sheba: Near-surface conditions and surface energy budget. *Journal of Geophysical Research: Oceans*, *107*(C10), SHE–21.

Persson, P. O. G., Uttal, T., Intrieri, J., Fairall, C., Andreas, E., & Guest, P. (1999). Observations of large thermal transitions during the arctic night from a suite of sensors at sheba. In *Preprints, fifth conference on polar meteorology and oceanography* (pp. 10–15).

Philipp, D., Stengel, M., & Ahrens, B. (2020). Analyzing the arctic feedback mechanism between sea ice and low-level clouds using 34 years of satellite observations. *Journal of Climate*, *33*(17), 7479 - 7501. Retrieved from https://journals.ametsoc.org/view/journals/clim/33/17/jcliD190895.xml doi: https://doi.org/10.1175/JCLI-D-19-0895.1

Pilz, C., Lonardi, M., Egerer, U., Siebert, H., Ehrlich, A., Heymsfield, A. J., ... Wendisch, M. (2023). Profile observations of the arctic atmospheric boundary layer with the beluga tethered balloon during mosaic. *Scientific Data*, *10*(1), 534.

Pincus, R., & Stevens, B. (2009). Monte carlo spectral integration: a consistent approximation for radiative transfer in large eddy simulations. *Journal of Advances in Modeling Earth Systems*, *1*(2). doi: https://doi.org/10.3894/JAMES.2009.1.1

Pithan, F., Ackerman, A., Angevine, W. M., Hartung, K., Ickes, L., Kelley, M., ... Zadra, A. (2016). Select strengths and biases of models in representing the arctic winter boundary layer over sea ice: the larcform 1 single column model intercomparison. *Journal of Advances in Modeling Earth Systems*, *8*(3), 1345-1357. Retrieved from https://agupubs.onlinelibrary.wiley.com/doi/abs/10.1002/2016MS000630 doi: https://doi.org/10.1002/2016MS000630

Pithan, F., & Mauritsen, T. (2014). Arctic amplification dominated by temperature feedbacks in contemporary climate models. *Nat. Geosci.*, *7*, 181–184. (https://doi.org/10.1038/ngeo2071) doi: 10.1038/ngeo2071

Pithan, F., Medeiros, B., & Mauritsen, T. (2014). Mixed-phase clouds cause climate model biases in arctic wintertime temperature inversions. *Clim. Dyn.*, *43*(1-2), 289-303. Retrieved from http://dx.doi.org/10.1007/s00382-013-1964-9 (https://doi.org/10.1007/s00382-013-1964-9) doi: 10.1007/s00382-013-1964-9

Pruppacher, H., & Klett, J. (1996). *Microphysics of clouds and precipitation*. Springer Netherlands. Retrieved from https://books.google.de/books?id=1mXN_qZ5sNUC

Rabe, B., Heuzé, C., Regnery, J., Aksenov, Y., Allerholt, J., Athanase, M., ... Zhu, J. (2022, February). Overview of the MOSAiC expedition: Physical oceanography. *Elem Sci Anth*, *10*(1), 00062. Retrieved 2023-

10-10, from https://online.ucpress.edu/elementa/article/10/1/00062/119792/Overview-of-the-MOSAiC-expedition-Physical doi: 10.1525/elementa.2021.00062

Randall, D. A., & Cripe, D. G. (1999). Alternative methods for specification of observed forcing in single-column models and cloud system models. *Journal of Geophysical Research: Atmospheres*, *104*(D20), 24527–24545.

Rantanen, M., Karpechko, A. Y., Lipponen, A., Nordling, K., Hyvärinen, O., Ruosteenoja, K., … Laaksonen, A. (2022). The arctic has warmed nearly four times faster than the globe since 1979. *Communications Earth & Environment*, *3*(1), 168.

Reisner, J., Rasmussen, R. M., & Bruintjes, R. T. (1998). Explicit forecasting of supercooled liquid water in winter storms using the mm5 mesoscale model. *Quarterly Journal of the Royal Meteorological Society*, *124*(548), 1071-1107. Retrieved from https://rmets.onlinelibrary.wiley.com/doi/abs/10.1002/qj.49712454804 doi: 10.1002/qj.49712454804

Riihimaki, L. (2021). *Radiation instruments on ice (iceradriihimaki).* doi: 10.5439/1608608

Ryan, B. F. (2000). A bulk parameterization of the ice particle size distribution and the optical properties in ice clouds. *Journal of the Atmospheric Sciences*, *57*(9), 1436 - 1451. Retrieved from https://journals.ametsoc.org/view/journals/atsc/57/9/1520-0469_2000_057_1436_abpoti_2.0.co_2.xml doi: 10.1175/1520-0469(2000)057⟨1436:ABPOTI⟩2.0.CO;2

Sandu, I., & Stevens, B. (2011). On the factors modulating the stratocumulus to cumulus transitions. *Journal of the Atmospheric Sciences*, *68*(9), 1865 - 1881. Retrieved from https://journals.ametsoc.org/view/journals/atsc/68/9/2011jas3614.1.xml doi: https://doi.org/10.1175/2011JAS3614.1

Schalkwijk, J., Jonker, H. J. J., Siebesma, A. P., & Bosveld, F. C. (2015). A year-long large-eddy simulation of the weather over cabauw: An overview. *Mon. Weather Rev.*, *143*(3), 828-844. doi: 10.1175/MWR-D-14-00293.1

Schemann, V., & Ebell, K. (2020). Simulation of mixed-phase clouds with the icon-lem in the complex arctic environment around ny–ålesund. *Atmos. Chem. Phys.*, *20*, 475-485. Retrieved from https://doi.org/10.5194/acp-20-475-2020 (https://doi.org/10.5194/acp-20-475-2020) doi: 10.5194/acp-20-475-2020

Screen, J. A., & Simmonds, I. (2010, April). The central role of diminishing sea ice in recent Arctic temperature amplification. *Nature*, *464*(7293), 1334–1337. Retrieved 2023-09-29, from https://www.nature.com/articles/nature09051 doi: 10.1038/nature09051

Seifert, A., & Beheng, K. D. (2006). A two-moment cloud microphysics parameterization for mixed-phase clouds. part 1: Model description. *Meteor. Atmos. Phys.*, *92*(1–2), 45-66. Retrieved from http://dx.doi.org/10.1007/s00703-005-0112-4 doi: 10.1007/s00703-005-0112-4

Serreze, M. C., & Barry, R. C. (2011). Processes and impacts of arctic amplification: A research synthesis. *Global Planet. Change*, *77*, 85-96. (https://doi.org/10.1016/j.gloplacha.2011.03.004) doi: 10.1016/j.gloplacha.2011.03.004

Shupe, M. D. (2011). Clouds at arctic atmospheric observatories. part ii: Thermodynamic phase characteristics. *Journal of Applied Meteorology and Climatology*, *50*(3), 645 - 661. Retrieved from https://journals.ametsoc.org/view/journals/apme/50/3/2010jamc2468.1.xml doi: https://doi.org/10.1175/2010JAMC2468.1

Shupe, M. D., & Intrieri, J. M. (2004). Cloud radiative forcing of the Arctic surface: The influence of cloud properties, surface albedo, and solar zenith angle. *J. Clim.*, *17*(3), 616–628. doi: 10.1175/1520-0442(2004)017⟨0616:CRFOTA⟩2.0.CO;2

Shupe, M. D., Matrosov, S. Y., & Uttal, T. (2006). Arctic mixed-phase cloud properties derived from surface-based sensors at sheba. *Journal of the Atmospheric Sciences*, *63*(2), 697 - 711. Retrieved from `https://journals.ametsoc.org/view/journals/atsc/63/2/jas3659.1.xml` doi: https://doi.org/10.1175/JAS3659.1

Shupe, M. D., Persson, P. O. G., Brooks, I. M., Tjernstrom, M., Sedlar, J., Mauritsen, T., ... Leck, C. (2013). Cloud and boundary layer interactions over the arctic sea ice in late summer. *Atmos. Chem. Phys.*, *13*, 9379-9399. doi: 10.5194/acp-13-9379-2013

Shupe, M. D., Rex, M., Blomquist, B., Persson, P. O. G., Schmale, J., Uttal, T., ... Yue, F. (2022, 02). Overview of the MOSAiC expedition: Atmosphere. *Elementa: Science of the Anthropocene*, *10*(1). Retrieved from `https://doi.org/10.1525/elementa.2021.00060` (00060) doi: 10.1525/elementa.2021.00060

Shupe, M. D., Rex, M., Dethloff, K., Damm, E., Fong, A. A., Gradinger, R., ... Sommerfeld, A. (2020). Arctic Report Card 2020: The MOSAiC Expedition: A Year Drifting with the Arctic Sea Ice. *Arctic Report Card*. Retrieved 2023-10-10, from `https://repository.library.noaa.gov/view/noaa/27898` doi: 10.25923/9G3V-XH92

Shupe, M. D., Turner, D. D., Zwink, A., Thieman, M. M., Mlawer, E. J., & Shippert, T. (2015). Deriving arctic cloud microphysics at barrow, alaska: Algorithms, results, and radiative closure. *Journal of Applied Meteorology and Climatology*, *54*(7), 1675 - 1689. Retrieved from `https://journals.ametsoc.org/view/journals/apme/54/7/jamc-d-15-0054.1.xml` doi: https://doi.org/10.1175/JAMC-D-15-0054.1

Siebesma, A. P., Bretherton, C. S., Brown, A., Chlond, A., Cuxart, J., Duynkerke, P. G., ... Stevens, D. E. (2003). A large eddy simulation intercomparison study of shallow cumulus convection. *J. Atmos. Sci.*, *60*, 1201-1219. doi: 10.1175/1520-0469(2003)60⟨1201:ALESIS⟩2.0.CO;2

Sobel, A. H., & Bretherton, C. S. (2000). Modeling tropical precipitation in a single column. *Journal of climate*, *13*(24), 4378–4392.

Solomon, A., Shupe, M. D., Persson, P. O. G., & Morrison, H. (2011). Moisture and dynamical interactions maintaining decoupled arctic mixed-phase stratocumulus in the presence of a humidity inversion. *Atmos. Chem. Phys.*, *11*(19), 10127–10148. doi: 10.5194/acp-11-10127-2011

Solomon, A., Shupe, M. D., Svensson, G., Barton, N. P., Batrak, Y., Bazile, E., ... Tolstykh, M. (2023, 04). The winter central Arctic surface energy budget: A model evaluation using observations from the MOSAiC campaign. *Elementa: Science of the Anthropocene*, *11*(1), 00104. Retrieved from `https://doi.org/10.1525/elementa.2022.00104` doi: 10.1525/elementa.2022.00104

Spreen, G., Kaleschke, L., & Heygster, G. (2008). Sea ice remote sensing using AMSR-E 89-GHz channels. *J. Geophys. Res.*, *113*, C02S03. doi: 10.1029/2005JC003384

Stevens, R. G., Loewe, K., Dearden, C., Dimitrelos, A., Possner, A., Eirund, G. K., ... Field, P. R. (2018). A model intercomparison of ccn-limited tenuous clouds in the high arctic. *Atmos. Chem. Phys.*, *18*(15), 11041-11071. doi: 10.5194/acp-18-11041-2018

Stramler, K., Del Genio, A., & Rossow, W. B. (2011). Synoptically driven arctic winter states. *J. Clim.*, *47*, 1747–1762. doi: 10.1175/2010JCLI3817.1

Stuecker, M. F., Bitz, C. M., Armour, K. C., Proistosescu, C., Kang, S. M., Xie, S.-P., ... Jin, F.-F. (2018, December). Polar amplification dominated by local forcing and feedbacks. *Nature Climate Change*, *8*(12), 1076–1081. Retrieved 2023-09-29, from `https://www.nature.com/articles/s41558-018-0339-y` doi: 10.1038/s41558-018-0339-y

Sverdrup, H. (1933). *The norwegian north polar expedition with the "maud", 1918-*

1925 : scientific results. Geofysisk Institutt, in co-operation with other institutions and A. S. John Griegs Boktrykkeri).

Taylor, P. C., Hegyi, B. M., Boeke, R. C., & Boisvert, L. N. (2018). On the increasing importance of air-sea exchanges in a thawing arctic: A review. *Atmosphere*, *9*(2). Retrieved from `https://www.mdpi.com/2073-4433/9/2/41` doi: 10.3390/atmos9020041

Tetens, O. (1930). über einige meteorologische begriffe. *Z. geophys*, *6*, 297–309.

Thackeray, C. W., & Hall, A. (2019, December). An emergent constraint on future Arctic sea-ice albedo feedback. *Nature Climate Change*, *9*(12), 972–978. Retrieved 2023-09-29, from `https://www.nature.com/articles/s41558-019-0619-1` doi: 10.1038/s41558-019-0619-1

van der Linden, S., & Ansorge, C. (2022, May). The coldest days of MOSAiC - an LES study. In *Egu general assembly conference abstracts* (p. EGU22-9646). doi: 10.5194/egusphere-egu22-9646

Van der Dussen, J., De Roode, S., Ackerman, A., Blossey, P., Bretherton, C., Kurowski, M., ... Siebesma, A. (2013). The gass/euclipse model intercomparison of the stratocumulus transition as observed during astex: Les results. *Journal of Advances in Modeling Earth Systems*, *5*(3), 483–499.

van der Linden, S. J. A., van de Wiel, B. J. H., Petenko, I., van Heerwaarden, C. C., Baas, P., & Jonker, H. J. J. (2020). A businger mechanism for intermittent bursting in the stable boundary layer. *Journal of the Atmospheric Sciences*, *77*(10), 3343 - 3360. Retrieved from `https://journals.ametsoc.org/view/journals/atsc/77/10/jasD190309.xml` doi: https://doi.org/10.1175/JAS-D-19-0309.1

van Laar, T. W., Schemann, V., & Neggers, R. A. J. (2019). Investigating the diurnal evolution of the cloud size distribution of continental cumulus convection using multi-day les. *J. Atmos. Sci.*. doi: 10.1175/JAS-D-18-0084.1

Wagner, D. N., Shupe, M. D., Cox, C., Persson, O. G., Uttal, T., Frey, M. M., ... Lehning, M. (2022). Snowfall and snow accumulation during the mosaic winter and spring seasons. *The Cryosphere*, *16*(6), 2373–2402. Retrieved from `https://tc.copernicus.org/articles/16/2373/2022/` doi: 10.5194/tc-16-2373-2022

Waliser, D. E., Li, J.-L. F., L'Ecuyer, T. S., & Chen, W.-T. (2011). The impact of precipitating ice and snow on the radiation balance in global climate models. *Geophysical Research Letters*, *38*(6). Retrieved from `https://agupubs.onlinelibrary.wiley.com/doi/abs/10.1029/2010GL046478` doi: https://doi.org/10.1029/2010GL046478

Wang, Y., Su, H., Jiang, J. H., Xu, F., & Yung, Y. L. (2020). Impact of cloud ice particle size uncertainty in a climate model and implications for future satellite missions. *Journal of Geophysical Research: Atmospheres*, *125*(6), e2019JD032119. Retrieved from `https://agupubs.onlinelibrary.wiley.com/doi/abs/10.1029/2019JD032119` (e2019JD032119 2019JD032119) doi: https://doi.org/10.1029/2019JD032119

Wendisch, M., Brückner, M., Crewell, S., Ehrlich, A., Notholt, J., Lüpkes, C., ... Zeppenfeld, S. (2023). Atmospheric and surface processes, and feedback mechanisms determining arctic amplification: A review of first results and prospects of the (ac)3 project. *Bulletin of the American Meteorological Society*, *104*(1), E208 - E242. Retrieved from `https://journals.ametsoc.org/view/journals/bams/104/1/BAMS-D-21-0218.1.xml` doi: https://doi.org/10.1175/BAMS-D-21-0218.1

Wyngaard, J. C. (2004). Toward numerical modeling in the "terra incognita". *Journal of the atmospheric sciences*, *61*(14), 1816–1826.

Yang, P., & Fu, Q. (2009). Dependence of ice crystal optical properties on particle aspect ratio. *Journal of Quantitative Spectroscopy and Radiative Transfer*, *110*(14), 1604-1614. Retrieved from `https://www.sciencedirect.com/`

science/article/pii/S0022407309000958 (XI Conference on Electromagnetic and Light Scattering by Non-Spherical Particles: 2008) doi: https://doi.org/10.1016/j.jqsrt.2009.03.004

Zhang, M., Bretherton, C. S., Blossey, P. N., Austin, P. H., Bacmeister, J. T., Bony, S., . . . Zhao, M. (2013). Cgils: Results from the first phase of an international project to understand the physical mechanisms of low cloud feedbacks in single column models. *Journal of Advances in Modeling Earth Systems*, *5*(4), 826-842. Retrieved from https://agupubs.onlinelibrary.wiley.com/doi/abs/10.1002/2013MS000246 doi: https://doi.org/10.1002/2013MS000246